

A Doublet-Lattice Method for Calculating Lift Distributions on Planar and Non-Planar Configurations in Subsonic Flows

Andrea Da Ronch^{1,2}, Luca Cavagna²

May 2007

Abstract

The Doublet-Lattice Method (DLM) is a collocation method for computing approximate solutions to the integral equation relating normalwash and aerodynamic loading for lifting surfaces oscillating harmonically in subsonic flows. Because the lifting surfaces are approximated by discrete lifting elements with trapezoidal geometry, the method permits straightforward analysis of planar and non-planar configurations. The lifting element consists of an oscillatory doublet line in conjunction with a horseshoe vortex; the horseshoe vortex represents the steady flow effects and the doublet represents the incremental effect of oscillatory motion. In the present work only the unsteady aerodynamic forces are required for dynamic aeroelastic calculations such as flutter analysis or dynamic response to external forces. Thus only the doublet singularities are used while for steady calculations a Vortex Lattice Method is directly adopted.

The present paper describes the results obtained using the computer program developed in the period April-May 2007.

¹ Department of Aeronautical and Vehicle Engineering, KTH - Sweden

² Department of Aerospace Engineering, Politecnico di Milano - Italy

Nomenclature

b	One half of the reference length, $c_r/2$
c_r	Reference length
CL	Total lift coefficient
CP	Pressure coefficient
e	Half width of a lifting surface element in the plane of the surface
h_0	Plunge mode amplitude, in a direction opposite to the local surface normal
F_z	Force coefficient in z-direction
F_y	Force coefficient in y-direction
i	Imaginary unit, $\sqrt{-1}$
K	Kernel function
k	Non-dimensional reduced frequency
M	Mach number
p	Lifting pressure coefficient
q	Dynamic pressure, $\rho U^2/2$
S	Reference surface
U	Free stream velocity
x, y, z	Cartesian coordinates of a receiving point
$\bar{x}, \bar{y}, \bar{z}$	Coordinates of a receiving point in a coordinate system aligned with a lifting surface element
w	Mode of the surface measured normal to the surface
y_0	Amplitude of the lateral displacement
Δx	Lifting surface element length in x-direction
λ	Sweep back angle of an element of a lifting surface
ξ, η, ζ	Cartesian coordinates of a sending point
$\bar{\xi}, \bar{\eta}, \bar{\zeta}$	Coordinates of a sending point in element coordinates ($\bar{\zeta}$ is always zero)
ω	Frequency of oscillation [rad/s]

Subscripts and Superscripts

r	Receiving point
s	Sending point

Introduction

The DLM is in use worldwide for flutter and dynamic analysis of aircraft at subsonic speeds. It is a classic tool for aeroelastic calculation which makes it de-facto the standard method for aeroelasticity in aerospace industry.

The paper presents the development of a computer program in MatLab® language for modeling oscillating interfering lifting surfaces in subsonic flows.

Approximate solutions from the linearized formulation are obtained by idealizing the surface as a set of lifting elements which are short line segments of acceleration-potential doublets. The classic well-known hypothesis assumed for irrotational and isoentropic flows are considered. The introduction of the acceleration potential enables to directly express a relationship between the downwash and the difference of pressure coefficient between the upper and lower side of a lifting surface. In this case it is correct to speak of ΔCP rather than CP to be more correct.

With the DLM, no effort is undertaken to model the wake which is assumed as a streamline which cannot sustain any load; the drawback of this formulation respect to the velocity potential is given by a more complicated relation which accounts for the influence of all the singularities in a given point. This final contribution of velocity in a point is given by the integration along the aircraft surface of the so-called kernel function K .

The load on each element is determined by satisfying normal velocity boundary conditions at a set of points on the surface.

The present paper describes two approximations for the variation of the numerator of the incremental oscillatory kernel function across the span of the box bound vortex; the quadratic approximation was presented firstly by Albano and Rodden in 1969 (Reference [1]) and a further refinement for a quartic approximation of the kernel function described by Rodden, Taylor and McIntosh Jr. in 1998 (Reference [2]).

Applications are made to a number of planar and non-planar configurations. Influence of box and wing aspect ratios are presented in different ways. All the examples used to validate the computer program are taken from papers and *MSC/NASTRAN Aeroelastic Analysis User's Guide*.

The paper is mainly intended to present the results of the actual work and compare them with those results which are considered as reference results. However, it was not possible to avoid treating, although in a concise way, the theory beyond the Doublet-Lattice Method.

Thus, the actual paper contains a short introduction to the algorithm of DLM where the most mathematical approaches are left to the references (**Section 1**). All the formulas used here are to be considered essential for the following section, **Section 2**, dealing with results and comparisons. Finally, **Section 3** contains the conclusions on the work performed and a brief critical review of it.

Table of Contents

Abstract.....	1
Nomenclature.....	2
Introduction.....	3
Table of Contents.....	4
List of Figures.....	5
List of Tables.....	6
1. The Doublet-Lattice Method.....	7
1.1 Quadratic approximation of the kernel function.....	9
<i>1.1.1 Planar and Non-Planar normalwash factors.....</i>	<i>10</i>
1.2 Quartic approximation of the kernel function.....	11
<i>1.2.1 Planar and Non-Planar normalwash factors.....</i>	<i>12</i>
2 Comparisons of the present computer program.....	13
2.1 Blaircraft 2100 Attack Fighter wing,.....	14
2.2 AGARD, candidate configuration I.-WING 445.6,.....	16
2.3 A 15-degrees sweptback wing in a wind tunnel,.....	18
2.4 Rectangular AR = 2 wing,.....	20
<i>2.4.1 Rectangular wing, 5 chord wise boxes (box AR = 0.5).....</i>	<i>21</i>
<i>2.4.2 Rectangular wing, 10 chord wise boxes (box AR = 1.0).....</i>	<i>23</i>
<i>2.4.3 Rectangular wing, 20 chord wise boxes (box AR = 2.0).....</i>	<i>25</i>
<i>2.4.4 Rectangular wing, 50 chord wise boxes (box AR = 5.0).....</i>	<i>27</i>
2.5 Rectangular wing, 20 equal-width strips, 20 equal-chord boxes,.....	29
<i>2.5.1 Rectangular AR = 2 wing, box AR = 1.0.....</i>	<i>30</i>
<i>2.5.2 Rectangular AR = 4 wing, box AR = 2.0.....</i>	<i>32</i>
<i>2.5.3 Rectangular AR = 6 wing, box AR = 3.0.....</i>	<i>34</i>
<i>2.5.4 Rectangular AR = 10 wing, box AR = 5.0.....</i>	<i>36</i>
2.6 FSW airplane in level flight,.....	38
2.7 FSW airplane in antisymmetric maneuvres,.....	39
2.8 Generalized Influence Matrix.....	40
3 Conclusions.....	45
References.....	46

List of Figures

List of Tables

1. The Doublet-Lattice Method

The flow singularities used to model the lifting surface are steady horseshoe vortices and oscillatory doublets along the bound vortex. At zero frequency, the doublet line corresponds to the horseshoe vortex. The vortices represent the steady-flow effects and the doublets the incremental effects of oscillatory motion. The vortex system can be analyzed exactly while the doublet system can only be approximated. In the subsequent sections, two types of approximation are used.

The configuration is modeled by dividing the surface into small trapezoidal elements (boxes) arranged in strips parallel to the free stream. Two edges of the boxes are always parallel to the free stream. To represent steady-flow effect, a horseshoe vortex is placed on each of the boxes in such a way the bound line coincides with the quarter-chord line of the box. To represent the oscillatory increment, a distribution of acceleration potential doublets of uniform strength, which have the steady-flow doublet strength subtracted, is superimposed on the bound vortex.

The surface boundary condition is applied at the control point of each box, centered spanwise on the three-quarter line of the box (**Figure 1**).

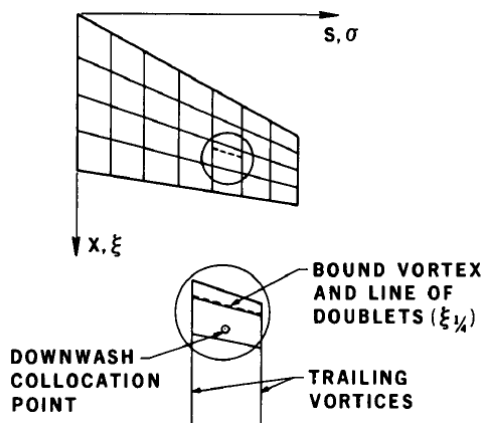


Figure 1. Surface idealization into boxes.

The linearized formulation of the oscillatory, subsonic, lifting surface theory relates the total dimensionless normalwash, w , at the surface to the lifting pressure coefficient, $p = (p_{\text{lower}} - p_{\text{upper}})/q$, across the surface. In matrix notation

$$\{w\} = [D]\{p\} \quad (1)$$

where D is the normalwash factor from the combined effects of the steady vortices and the oscillatory doublets.

The influences of all vortices and doublets, indexed by the subscript s (for sending), are summed for each control point, indexed by the subscript r (for receiving), to get

$$w_r = \sum_s D_{rs} p_s \quad (2)$$

where $D_{rs} = D_{0,rs} + D_{1,rs} + D_{2,rs}$ is the sum of the steady normalwash factor, $D_{0,rs}$, and the incremental oscillatory normalwash, divided for convenience in the planar, $D_{1,rs}$, and non-planar term, $D_{2,rs}$.

By transforming the coordinate system to the midpoint of the sending line and align it with the plane of the sending box (see **Figure 2**: local ξ -axis is aligned with the free stream, local ζ -axis is normal to the surface box and local η -axis from right-hand rule.), the normalwash factors appear as

$$D_{0,rs} = \frac{\Delta x_s}{8\pi} \int_{-e}^e \left(\frac{K_{10} T_1}{r_1^2} + \frac{K_{20} T_2^*}{r_1^4} \right) d\bar{\eta} \quad (3)$$

$$D_{1,rs} = \frac{\Delta x_s}{8\pi} \int_{-e}^e \left(\frac{\{K_1 \exp[-i\omega(\bar{x} - \bar{\eta} \tan \lambda_s)/U] - K_{10}\} T_1}{r_1^2} \right) d\bar{\eta} \quad (4)$$

$$D_{2,rs} = \frac{\Delta x_s}{8\pi} \int_{-e}^e \left(\frac{\{K_2 \exp[-i\omega(\bar{x} - \bar{\eta} \tan \lambda_s)/U] - K_{20}\} T_2^*}{r_1^4} \right) d\bar{\eta} \quad (5)$$

where the bar denotes the local coordinates at the sending box, ω is the frequency, U is the free stream velocity, Δx_s is the chord of the sending box, λ_s is the sweep angle of its quarter-chord and e is its semiwidth.

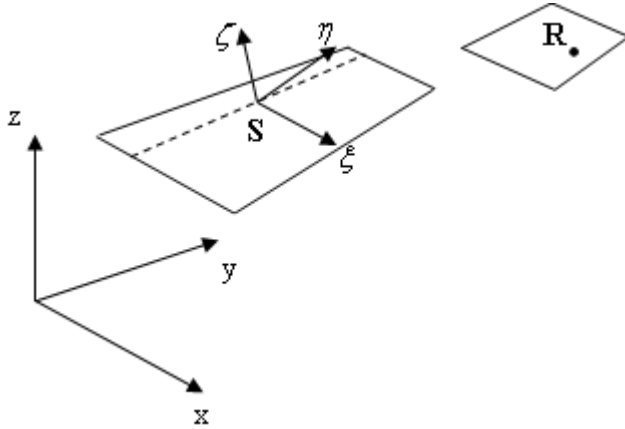


Figure 2. Local coordinate system at the sending box (S).

Moreover the following parameters are part of the integrand functions in expressions from (3) to (5):

the cylindrical radius from sending doublet

$$r_1 = [(\bar{y} - \bar{\eta})^2 + \bar{z}^2]^{1/2};$$

Rodemich's direction cosine function (Reference [3]) are

$$T_1 = \cos(\gamma_s - \gamma_r),$$

$$T_2^* = \bar{z}[\bar{z} \cos(\gamma_s - \gamma_r) + (\bar{y} - \bar{\eta}) \sin(\gamma_s - \gamma_r)],$$

where γ_r and γ_s are the dihedral angles at the receiving and sending box, respectively;

Landahl's forms of the kernel numerator (Reference [4]) are

$$\begin{aligned}
 K_1 &= -I_1 - \exp(-ik_1 u_1) Mr_1 / R (1+u_1^2)^{1/2}, \\
 K_2 &= 3I_2 + ik_1 \exp(-ik_1 u_1) (Mr_1/R)^2 (1+u_1^2)^{1/2} + \exp(-ik_1 u_1) Mr_1 [(1+u_1^2)(\beta r_1/R)^2 + 2 + Mr_1 u_1]; \\
 \beta &= (1-M^2)^{1/2}; \\
 R &= [(\bar{x} - \bar{\eta} \tan \lambda_s)^2 + (\beta r_1)^2]^{1/2}; \\
 u_1 &= (MR - \bar{x} + \bar{\eta} \tan \lambda_s) / \beta^2 r_1;
 \end{aligned}$$

the reduced frequency is

$$k_1 = \omega_r / U;$$

the steady values of K_1 and K_2 , denoted K_{10} and K_{20} are

$$\begin{aligned}
 K_{10} &= -1 - (\bar{x} - \bar{\eta} \tan \lambda_s) / R, \\
 K_{20} &= 2 + (\bar{x} - \bar{\eta} \tan \lambda_s) [2 + (\beta r_1/R)^2] / R;
 \end{aligned}$$

and the integrals

$$I_1 = \int_{u_1}^{\infty} (1+u^2)^{-3/2} \exp(-ik_1 u) du,$$

$$I_2 = \int_{u_1}^{\infty} (1+u^2)^{-5/2} \exp(-ik_1 u) du$$

are computed using Laschka's approximation (Appendix A of Reference [6]).

The boundary conditions of tangential flow are expressed as:

$$\alpha = \frac{\dot{w}}{U} + \frac{dw}{dx} = ik \frac{w}{b} + \frac{dw}{dx},$$

where $b = c_r/2$ is one half of the reference length.

The steady normalwash factor is not calculated from equation (3) but by utilizing the non-planar horseshoe vortex formulas of Hedman (Reference [5]). Instead, the incremental oscillatory normalwash factors are evaluated by approximating the numerators of the formulas (4) and (5) as described in **Section 1.1** and **1.2**.

1.1 Quadratic approximation of the kernel function

Expressions (4) and (5) are rewritten in the following way

$$D_{1,rs} = \frac{\Delta x_s}{8\pi} \int_{-e}^e \frac{P_1(\bar{\eta})}{(\bar{y} - \bar{\eta})^2 + \bar{z}^2} d\bar{\eta}$$

(6)

$$D_{2,rs} = \frac{\Delta x_s}{8\pi} \int_{-e}^e \frac{P_2(\bar{\eta})}{[(\bar{y} - \bar{\eta})^2 + \bar{z}^2]^2} d\bar{\eta} \quad (7)$$

where P_1 and P_2 are intended to be parabolic approximations of the numerator of the kernel function, depending on the local variable $\bar{\eta}$:

$$P_1(\bar{\eta}) = A_1 \bar{\eta}^2 + B_1 \bar{\eta} + C_1 \approx \{K_1 \exp[-i\omega(\bar{x} - \bar{\eta} \tan \lambda_s)/U] - K_{10}\} T_1 \quad (8)$$

$$P_2(\bar{\eta}) = A_2 \bar{\eta}^2 + B_2 \bar{\eta} + C_2 \approx \{K_2 \exp[-i\omega(\bar{x} - \bar{\eta} \tan \lambda_s)/U] - K_{20}\} T_2^* \quad (9)$$

If the inboard, center and outboard values of $P_1(\bar{\eta})$ are denoted by $P_1(-e)$, $P_1(0)$, $P_1(e)$, respectively, the parabolic coefficients of $P_1(\bar{\eta})$ are

$$A_1 = [P_1(-e) - 2P_1(0) + P_1(e)]/2e^2$$

$$B_1 = [P_1(e) - P_1(-e)]/2e$$

$$C_1 = P_1(0)$$

and, similarly for $P_2(\bar{\eta})$,

$$A_2 = [P_2(-e) - 2P_2(0) + P_2(e)]/2e^2$$

$$B_2 = [P_2(e) - P_2(-e)]/2e$$

$$C_2 = P_2(0)$$

Spanwise distribution for each box of the quadratic curve-fitting is shown in **Figure 3**.

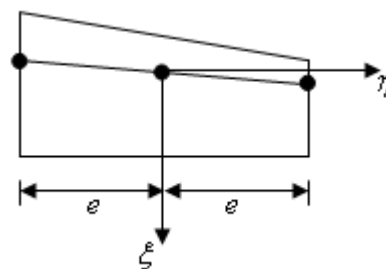


Figure 3. 3 evaluation points for quadratic coefficients.

1.1.1 Planar and Non-Planar normalwash factors

Once parabolic coefficients for the approximation of the numerator of the kernel functions in (8) and (9) have been computed, planar normalwash factors in (6) and non-planar normalwash factor in (7) can be determined using quite long formulas. These formulas are not reported in the present paper for convenience, but they can be found, i.e., at pages 4-7 and 4-8 of Reference [6].

1.2 Quartic approximation of the kernel function

Beside the original parabolic approximation, a higher order approximation is used to describe the span wise variation of the numerator of the incremental oscillatory kernel. Again, expressions in (4) and (5) are rewritten

$$D_{1,rs} = \frac{\Delta x_s}{8\pi} \int_{-e}^e \frac{Q_1(\bar{\eta})}{(\bar{y} - \bar{\eta})^2 + \bar{z}^2} d\bar{\eta} \quad (10)$$

$$D_{2,rs} = \frac{\Delta x_s}{8\pi} \int_{-e}^e \frac{Q_2(\bar{\eta})}{[(\bar{y} - \bar{\eta})^2 + \bar{z}^2]^2} d\bar{\eta} \quad (11)$$

where Q_1 and Q_2 are intended to be generic quartic polynomials. The following approximations hold

$$Q_1(\bar{\eta}) = A_1 \bar{\eta}^2 + B_1 \bar{\eta} + C_1 + D_1 \bar{\eta}^3 + E_1 \bar{\eta}^4 \approx \{K_1 \exp[-i\omega(\bar{x} - \bar{\eta} \tan \lambda_s)/U] - K_{10}\} T_1 \quad (12)$$

$$Q_2(\bar{\eta}) = A_2 \bar{\eta}^2 + B_2 \bar{\eta} + C_2 + D_2 \bar{\eta}^3 + E_2 \bar{\eta}^4 \approx \{K_2 \exp[-i\omega(\bar{x} - \bar{\eta} \tan \lambda_s)/U] - K_{20}\} T_2^* \quad (13)$$

If the inboard, inboard intermediate, center, outboard intermediate and outboard values of $Q_1(\bar{\eta})$ are denoted by $Q_1(-e), Q_1(-e/2), Q_1(0), Q_1(e/2), Q_1(e)$, respectively, the quartic coefficients of $Q_1(\bar{\eta})$ are

$$A_1 = -1/6e^2 [Q_1(-e) - 16Q_1(-e/2) + 30Q_1(0) - 16Q_1(e/2) + Q_1(e)]$$

$$B_1 = 1/6e [Q_1(-e) - 8Q_1(-e/2) + 8Q_1(e/2) - Q_1(e)]$$

$$C_1 = Q_1(0)$$

$$D_1 = -2/3e^3 [Q_1(-e) - 2Q_1(-e/2) + 2Q_1(e/2) - Q_1(e)]$$

$$E_1 = 2/3e^4 [Q_1(-e) - 4Q_1(-e/2) + 6Q_1(0) - 4Q_1(e/2) + Q_1(e)]$$

and, similarly for $Q_2(\bar{\eta})$,

$$A_2 = -1/6e^2 [Q_2(-e) - 16Q_2(-e/2) + 30Q_2(0) - 16Q_2(e/2) + Q_2(e)]$$

$$B_2 = 1/6e [Q_2(-e) - 8Q_2(-e/2) + 8Q_2(e/2) - Q_2(e)]$$

$$C_2 = Q_2(0)$$

$$D_2 = -2/3e^3 [Q_2(-e) - 2Q_2(-e/2) + 2Q_2(e/2) - Q_2(e)]$$

$$E_2 = 2/3e^4 [Q_2(-e) - 4Q_2(-e/2) + 6Q_2(0) - 4Q_2(e/2) + Q_2(e)].$$

Spanwise distribution for each box of the quartic curve-fitting is shown in **Figure 4**.

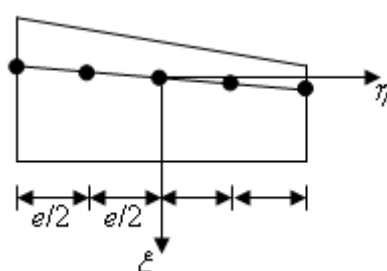


Figure 4. 5 evaluation points for quartic coefficients.

1.2.1 Planar and Non-Planar normalwash factors

The quartic coefficients, according to the above equations, are used to express planar and non-planar normalwash factors in (4) and (5), respectively. Formulas are not reported for convenience but they can be found at pages 722 and 723 of Reference [2].

2 Comparisons of the present computer program

The developed computer program is tested on several examples, with increasing complexity, in order to validate the present code. Moreover, the use of symmetry is a key point because it permits to reduce a model to one half, the right or the left one. So, it is very important to model correctly the case in which a vertical fin in the symmetry plane is present.

Wing geometrical properties and configuration types for all the comparisons are shown in **Table 1**:

Section	Geometry			Configuration	
	Sweep	Dihedral	Taper	Planar	Non-planar
2.1				X	
2.2	X		X	X	
2.3	X		X	X	
2.4				X	
2.5				X	
2.6	X				X
2.7	X	X			X
2.8	X		X	X	

Table 1. Model configurations for each section.

Moreover, **Section 2.4** presents a study on the influence of the box aspect ratio on the lift coefficient, while the following section, **2.5**, outlines the effect of a contemporary increase in the wing and box aspect ratio. The last section, **2.8**, uses the present computer program to calculate the generalized aerodynamic influence coefficient matrix for an AGARD standard aeroelastic configuration.

In **Section 2.2**, **2.3**, and **2.6** the subsonic stability derivative $C_{L,\alpha}$ is computed. According to Reference [19], it is defined in the following way

$$C_{L,\alpha} = \frac{b}{h_0^2 k S} \operatorname{Im}(F_z), \quad (14)$$

where $b = c_r/2$ is one half of the reference length; F_z is the force coefficient in z-direction; h_0 represents the plunge motion and in the examples $h_0 = 1$ to represent unitary plunge motion.

Instead, in **Section 2.7** the subsonic sideslip derivative $C_{Y,\beta}$ is calculated. According to Reference [19], it is formulated as

$$C_{Y,\beta} = \left(\frac{c_r}{2 y_0^2 k S} \right) \operatorname{Im}(F_y), \quad (15)$$

where F_y is the force coefficient in y-direction and y_0 represents the side motion along y-axis; in the example here presented, $y_0 = 1$ to consider unitary side motion along y-axis.

2.1 Blairst 2100 Attack Fighter wing,

from Reference [20].

The flat wing has an aspect ratio of 2, no taper, twist and sweep angle. It is divided into 18 boxes, 3 chord wise and 6 span wise. Only the right half span model is considered and pressure coefficient distribution over the 9 boxes is computed applying symmetrical conditions to take into account for the left half span wing which is not modeled. The complete wing configuration is shown in **Figure 5**, while geometrical and flight conditions are specified in **Table 2**.

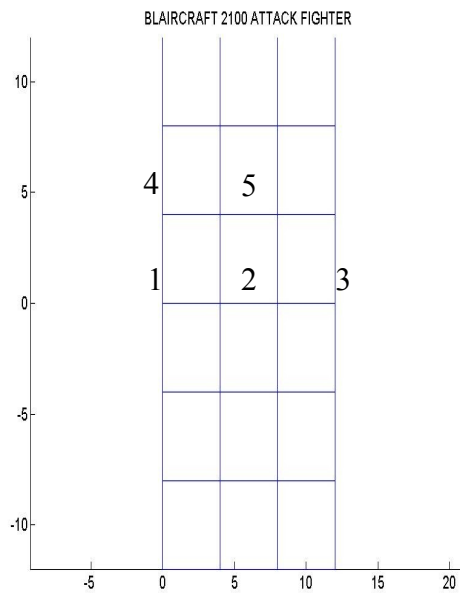


Figure 5. Blairst 2100 Attack Fighter wing layout.

<i>Geometrical properties</i>		
<i>Symbols</i>	<i>Values</i>	<i>Descriptions</i>
b [m]	12	chord
AR	2	aspect ratio
L _{ref} [m]	6	reference length
S _{ref} [m ²]	4	reference surface
<i>Flight conditions</i>		
<i>Symbols</i>	<i>Values</i>	<i>Descriptions</i>
M	0.5	Mach number
k	1	reduced frequency

Table 2. Data used to compute pressure coefficient distribution on the right half span model of Blairst 2100 Attack Fighter wing.

According to the reference paper, boundary conditions correspond to a plunge with magnitude equal to one (the imaginary part of the boundary condition equation is set to one). Both approximations, quadratic and quartic, have been tested on the right half model

considering symmetry and the following results computed (see **Table 3**). Results obtained by M. Blair are not reported for convenience because pressure coefficient distribution obtained with quadratic approximation is exactly the same of the reference.

box	Quadratic approximation		Quartic approximation	
	real(CP)	imag(CP)	real(CP)	imag(CP)
1	-5.4902e-001	+6.2682e+000	-5.6098e-001	+5.7936e+000
2	-3.8862e+000	+2.4495e+000	-3.5519e+000	+2.3119e+000
3	-3.8736e+000	+1.1745e+000	-3.5194e+000	+1.0961e+000
4	-5.9146e-001	+5.8092e+000	-5.9907e-001	+5.3863e+000
5	-3.6405e+000	+2.1530e+000	-3.3429e+000	+2.0434e+000
6	-3.6234e+000	+1.0281e+000	-3.3065e+000	+9.6176e-001
7	-5.8286e-001	+4.5474e+000	-5.8574e-001	+4.2488e+000
8	-2.8983e+000	+1.4663e+000	-2.6908e+000	+1.4079e+000
9	-2.8893e+000	+7.1185e-001	-2.6648e+000	+6.6740e-001

Table 3. Pressure coefficient distribution over the right half span model using quadratic and quartic approximation of the kernel numerator. Quadratic outputs are exactly equal to those shown in the reference paper.

Pressure coefficient distribution is shown in **Figure 6** for the quadratic approximation. Boxes are numbered from the leading edge backwards in row by row outwards (see **Figure 5**).

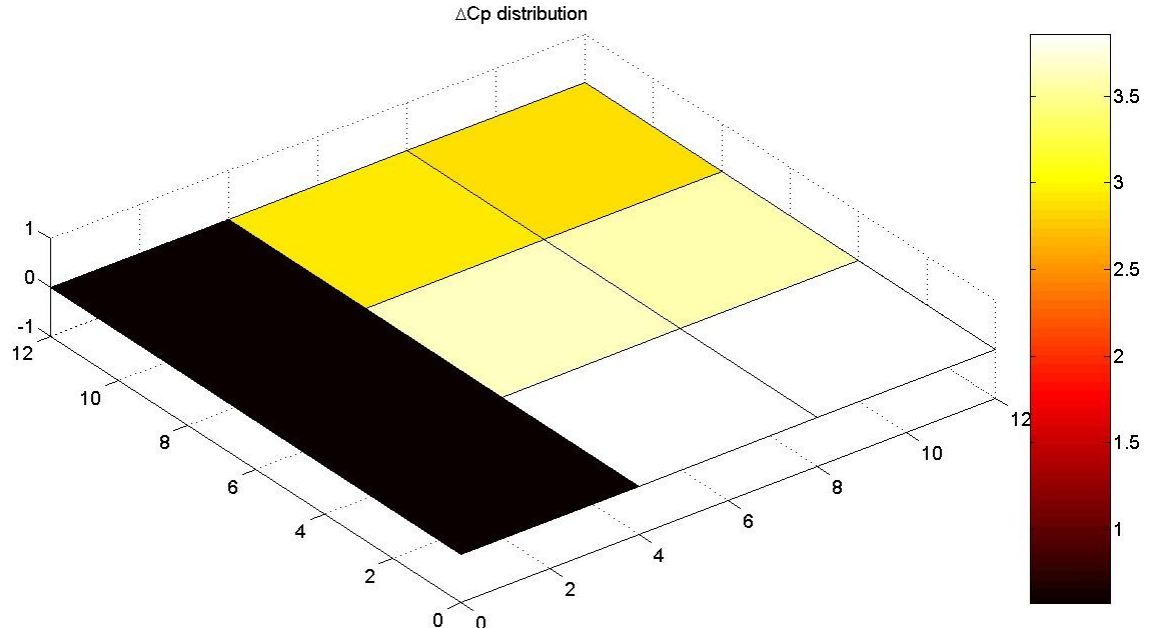


Figure 6. Pressure distribution over the right half span wing using quadratic approximation.

2.2 AGARD, candidate configuration I.-WING 445.6,

from Reference [14].

The flat wing with 45 degree of sweptback has taper but no dihedral angle and twist. The inboard chord is 0.557784in and the outboard chord 0.368199in, with a span of 0.762in. The wing is mounted in a wind tunnel for flutter tests and thus wall reflection is accounted through the use of symmetry. The wing is divided into 100 boxes, 10 chord wise and 10 span wise. Wing configuration is shown in **Figure 7.** and main parameters are in **Table 4.**

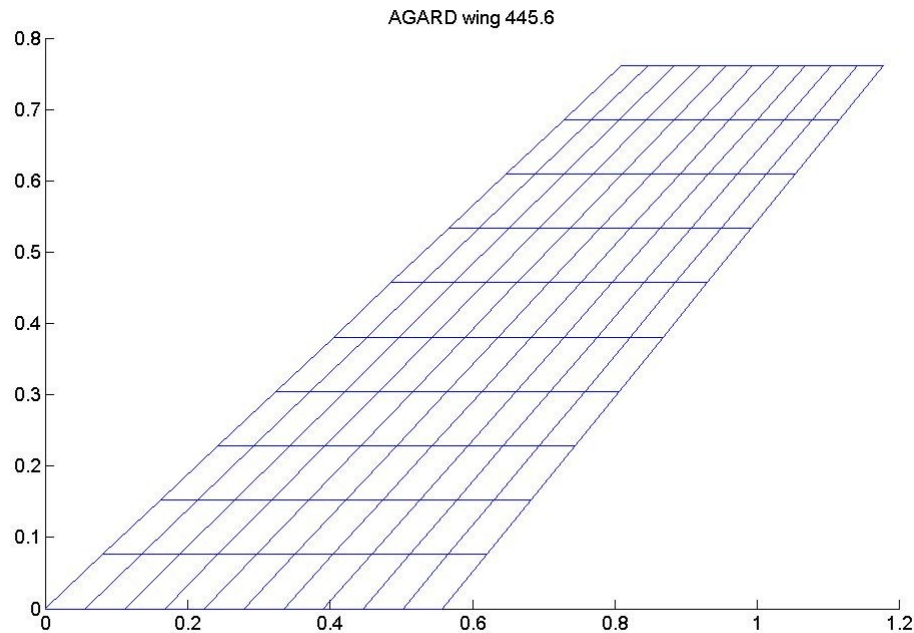


Figure 7. AGARD wing 445.6 layout.

<i>Geometrical properties</i>		
<i>Symbols</i>	<i>Values</i>	<i>Descriptions</i>
b_i [in]	0.557784	inboard chord
b_o [in]	0.368199	outboard chord
s [in]	0.762	span
L_{ref} [in]	0.4629915	reference length
S_{ref} [in^2]	0.3528	reference surface
Λ [deg]	45	sweep angle
<i>Flight conditions</i>		
<i>Symbols</i>	<i>Values</i>	<i>Descriptions</i>
M	0.5	Mach number
k	0.0001	reduced frequency

Table 4. Data used to compute subsonic derivative for AGARD wing 445.6.

Both approximations are used to compute the subsonic derivative $C_{L,\alpha}$, defined previously in equation 14 at page 13, and results are reported in **Table 5**. Because the paper

does not present this stability derivative, it was estimated using TORNADO. The corresponding pressure coefficient distribution is shown in **Figure 8.** for the quartic approximation.

	TORNADO	Quadratic approximation	Quartic approximation
$C_{L,\alpha}$	3.01	3.2392	3.1308

Table 5. Subsonic derivative for the rigid AGARD wing 445.6.

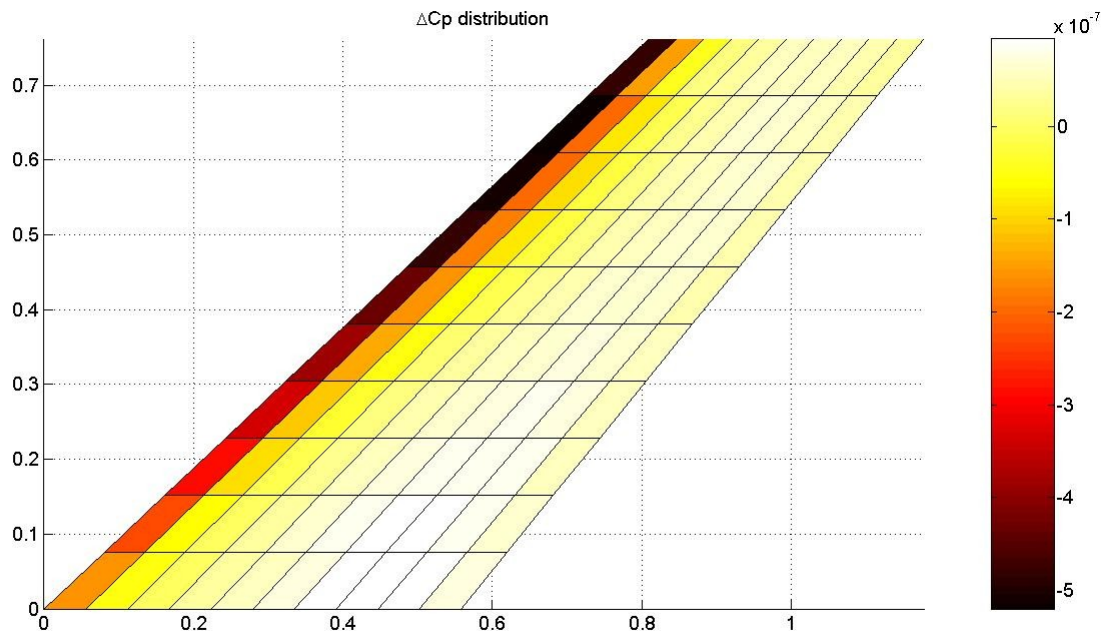


Figure 8. Pressure coefficient distribution over the AGARD wing 445.6 accounting for wall reflection in the wind tunnel.

2.3 A 15-degrees sweptback wing in a wind tunnel,

from Reference [19], Example HA144C.

The flat wing with 15 deg of sweepback has a constant chord of 2.07055in and a semi span of 5.52510in. It has no taper, twist and dihedral angle. The wing is divided into 24 boxes, 4 chord wise and 6 span wise. The wing is mounted in a wind tunnel for flutter at subsonic speed and wall reflection is taken into account through symmetry. Wing configuration is shown in **Figure 9** and parameters which have been used in **Table 6**.

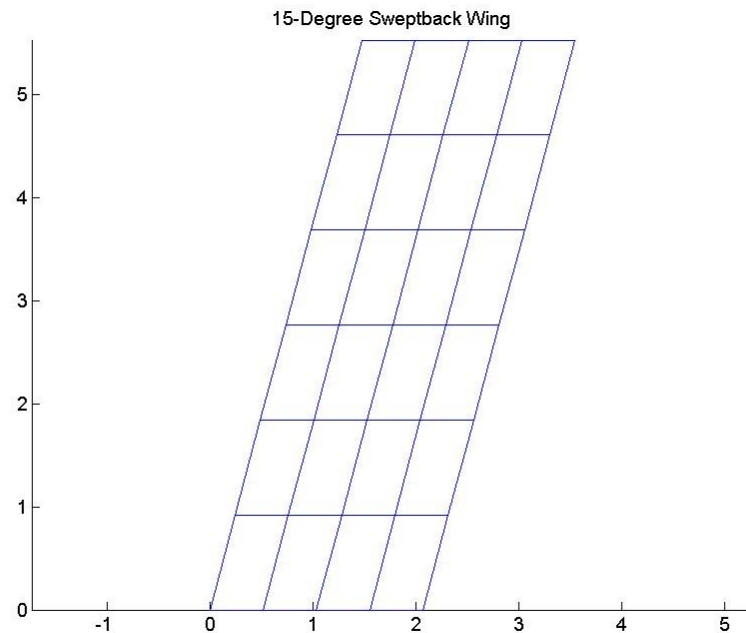


Figure 9. A 15-Degree sweptback wing layout.

<i>Geometrical properties</i>		
<i>Symbols</i>	<i>Values</i>	<i>Descriptions</i>
b [in]	2.07055	chord
s [in]	5.52510	span
L _{ref} [in]	2.07055	reference length
S _{ref} [in ²]	11.4399	reference surface
Λ [deg]	15	sweep angle
<i>Flight conditions</i>		
<i>Symbols</i>	<i>Values</i>	<i>Descriptions</i>
M	0.45	Mach number
k	0.0001	reduced frequency

Table 6. Data used to compute subsonic derivative for rigid wing.

Boundary conditions correspond to a plunge with deflection mode equal to one ($w = 1$). The subsonic derivative $C_{L,\alpha}$ is computed using both methods and the results compared with those presented in the reference, see **Table 7**.

	NASTRAN	TORNADO	Quadratic approximation	Quartic approximation
$C_{L,c}$	4.486	4.1858	4.8058	4.5105

Table 7. Subsonic derivative for a rigid 15 degree sweptback wing.

The corresponding pressure coefficient distribution is shown in **Figure 10** for the quartic approximation.

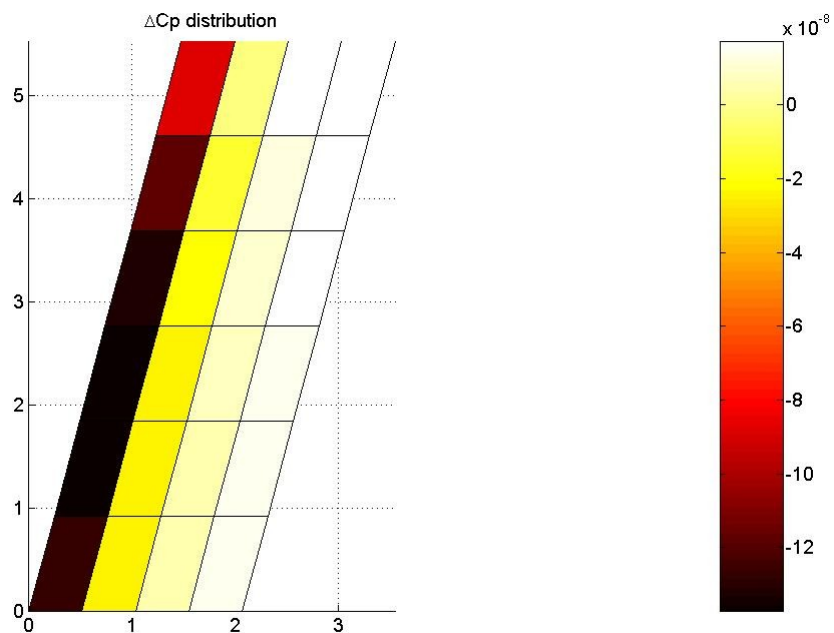


Figure 10. Pressure coefficient distribution over the 15 degree sweptback wing accounting for wall reflection.

2.4 Rectangular AR = 2 wing,

from Reference [8].

The flat rectangular wing has an aspect ratio equal to 2 and it is pitching about its mid chord at subsonic speed ($M = 0.8$). Only the right half span wing is modeled and is divided into 10 equal-width strips and each strip is divided into equal chord boxes from 5 to 50. The box ARs vary from 0.5 to 5. The reduced frequency dependence is also varied from 0.1 to 2.0.

The influence of box ARs on the total lift coefficient is investigated in function of the reduced frequency for a fixed wing AR. Symmetry is used through all the comparisons. In the following, results from the simulations are shown using data reported in **Table 8**.

<i>Geometrical properties</i>		
<i>Symbols</i>	<i>Numbers</i>	<i>Descriptions</i>
b [m]	1	chord
AR	2	aspect ratio
box AR	0.5, 1.0, 2.0, 5.0	box aspect ratio
L _{ref} [m]	1	reference length
S _{ref} [m ²]	2	reference surface
<i>Flight conditions</i>		
<i>Symbols</i>	<i>Numbers</i>	<i>Descriptions</i>
M	0.8	Mach number
k	0.1, 0.5, 1.0, 2.0	reduced frequencies

Table 8. Data used to compute total lift coefficients for a rectangular AR = 2 wing.

Total lift coefficients have been calculated using both approximations, quadratic and quartic, and these results are compared with the values provided by the authors in the reference paper, using the so-called N5KQ computer program.

Moreover, for each value of box AR the dependence of the total lift coefficient on the reduced frequency is shown because it was seen that the corresponding plot gives a clear indication of the differences between the present computer program and more sophisticated codes.

2.4.1 Rectangular wing, 5 chord wise boxes (box AR = 0.5).

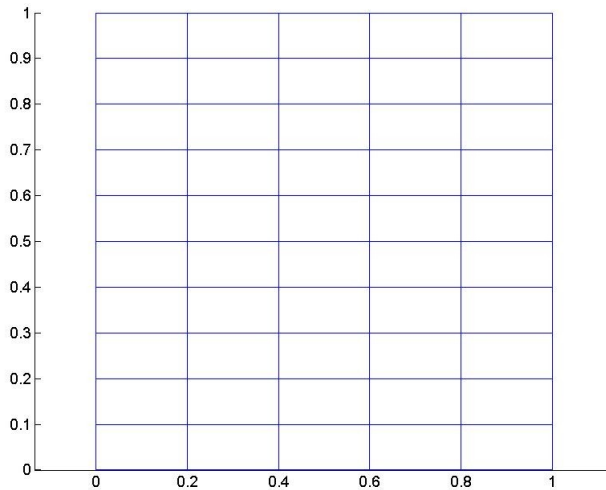


Figure 11. Rectangular wing, box AR = 0.5.

k	N5KQ		Quadratic approximation		Quartic approximation	
	real(CL)	imag(CL)	real(CL)	imag(CL)	real(CL)	imag(CL)
0.1	2.968	0.3626	2.9691	0.3634	2.9674	0.3656
0.5	3.638	1.739	3.6422	1.7418	3.6204	1.7605
1.0	4.492	1.823	4.4966	1.8207	4.4637	1.8733
2.0	4.652	2.380	4.6568	2.3775	4.5315	2.4436

Table 9. Total lift coefficient for a rectangular wing, box AR = 0.5.

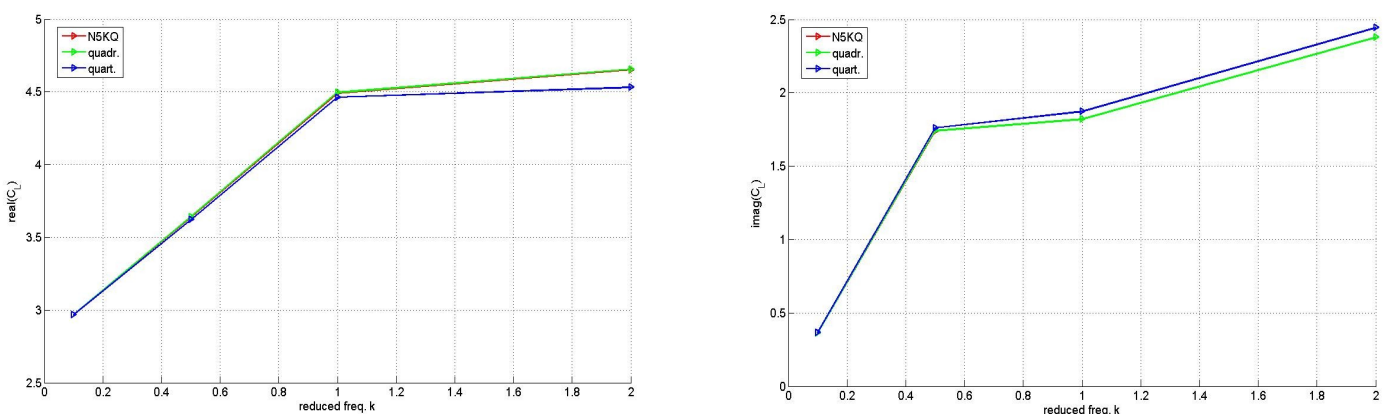


Figure 12. Real and imaginary part of the total lift coefficient, box AR = 0.5.

Lift Distributions on Planar and Non-Planar Configurations

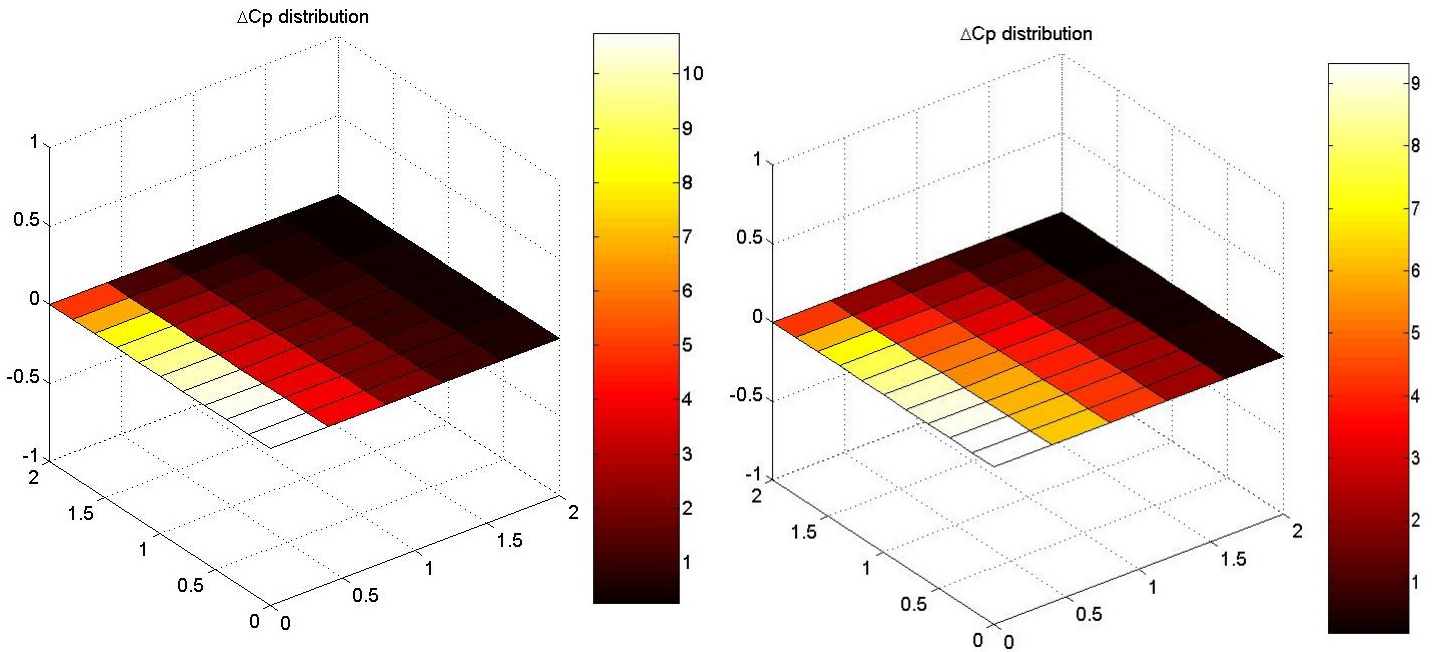


Figure 13. Pressure coefficient distribution using quartic approximation; on the left, reduced frequency is 0.1, on the right 0.5.

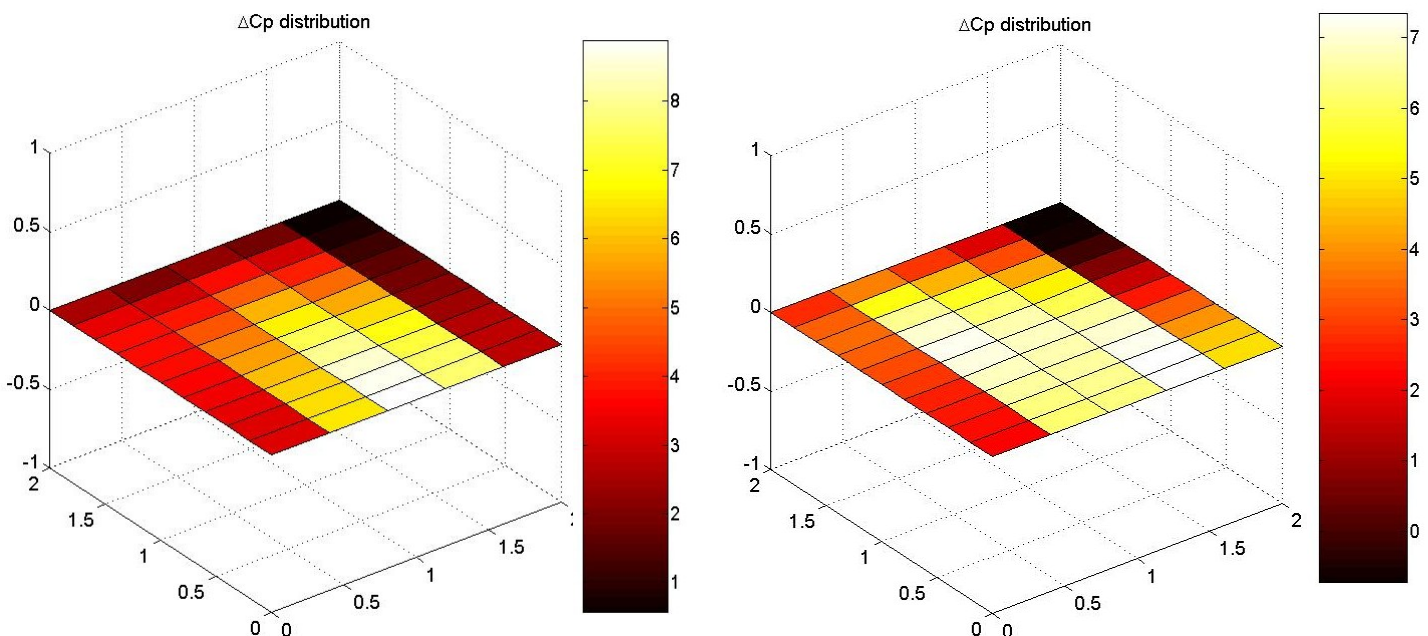


Figure 14. Pressure coefficient distribution using quartic approximation; on the left, reduced frequency is 1.0, on the right 2.0.

2.4.2 Rectangular wing, 10 chord wise boxes (box AR = 1.0).

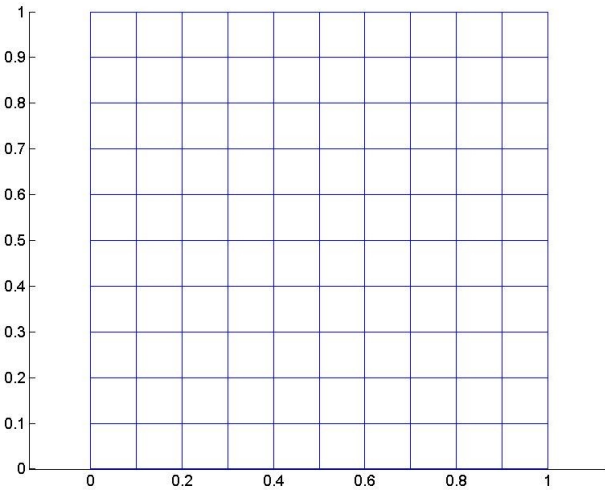


Figure 15. Rectangular wing, box AR = 1.0.

k	N5KQ		Quadratic approximation		Quartic approximation	
	real(CL)	imag(CL)	real(CL)	imag(CL)	real(CL)	imag(CL)
0.1	2.968	0.3565	2.9804	0.3699	2.9751	0.3681
0.5	3.770	1.724	3.8359	1.7494	3.8054	1.7539
1.0	4.768	1.528	4.8452	1.4669	4.8284	1.5027
2.0	5.396	1.814	5.4860	1.7126	5.4168	1.7774

Table 10. Total lift coefficient for a rectangular wing, box AR = 1.0.

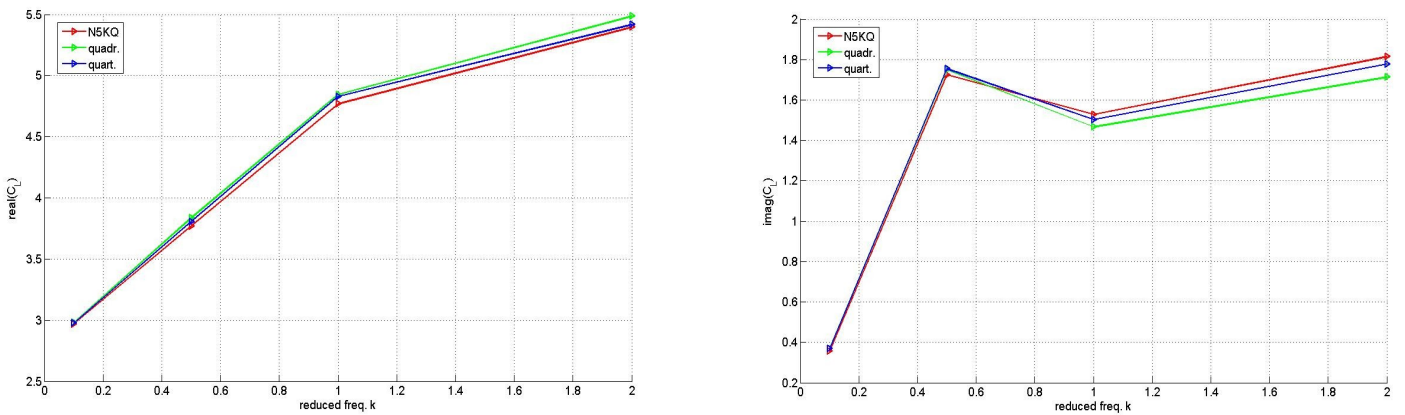


Figure 16. Real and imaginary part of the total lift coefficient, box AR = 1.0.

Lift Distributions on Planar and Non-Planar Configurations

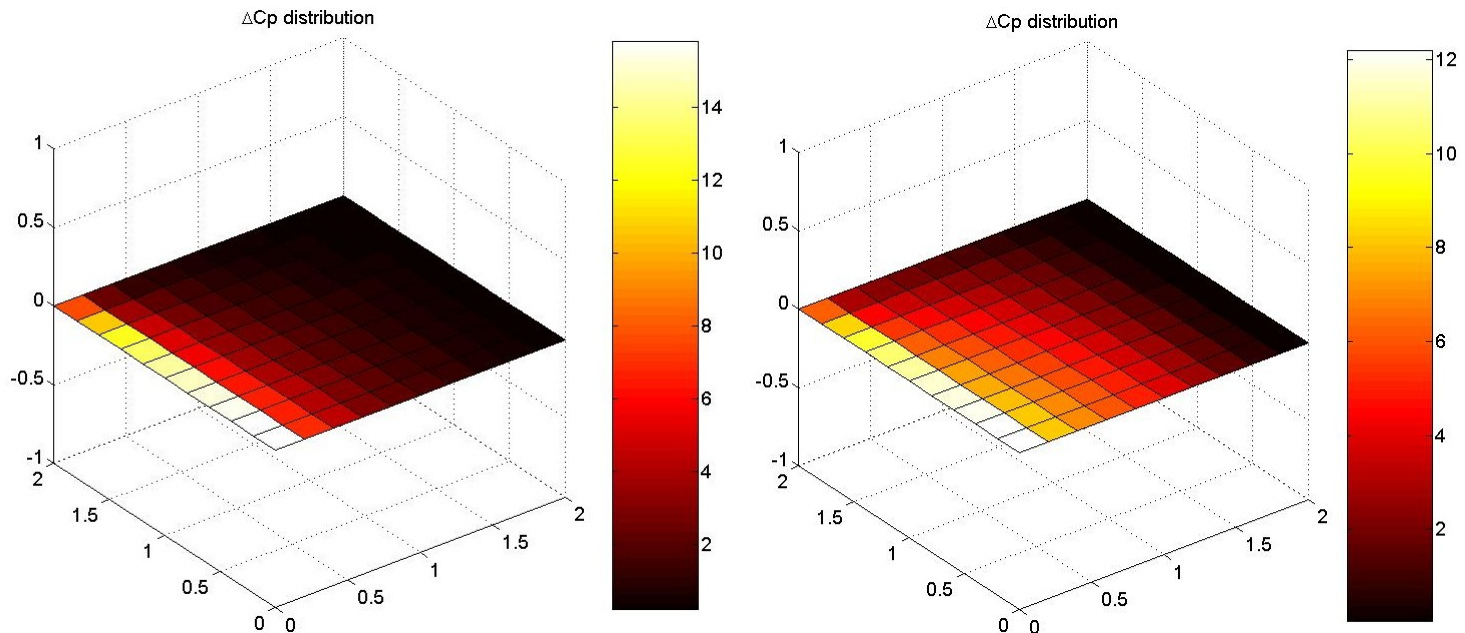


Figure 17. Pressure coefficient distribution using quartic approximation; on the left, reduced frequency is 0.1, on the right 0.5.

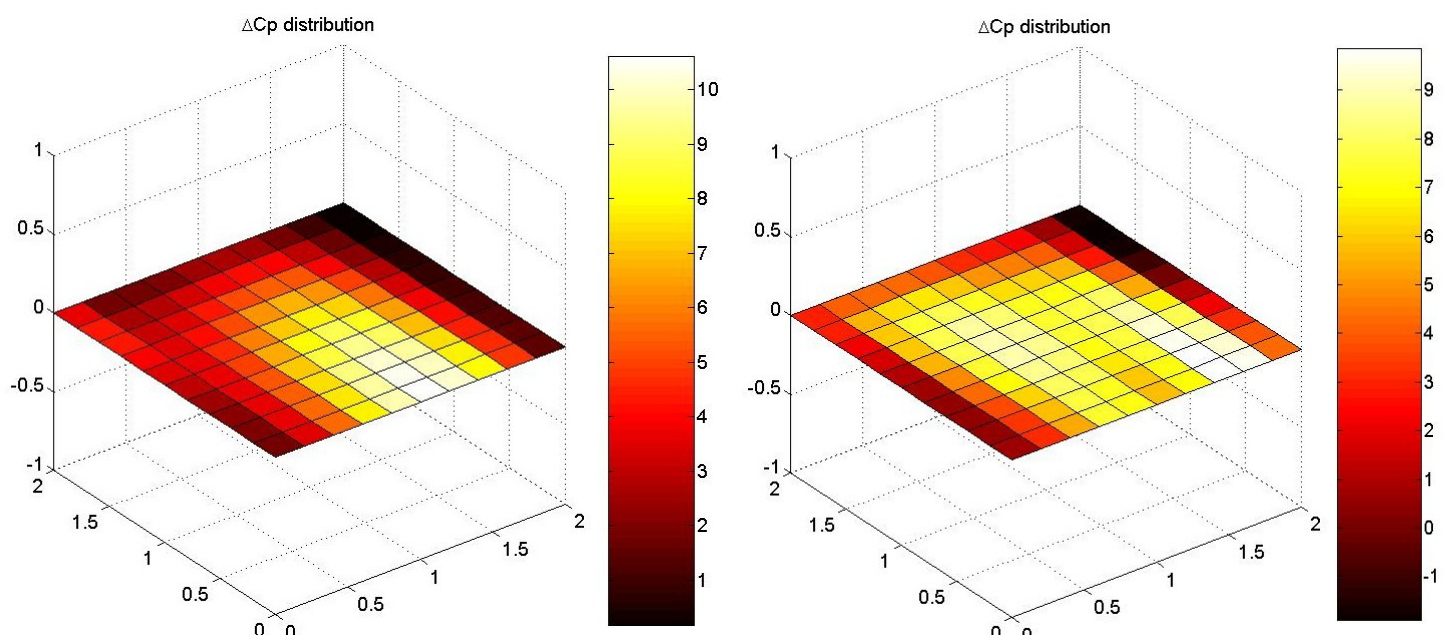


Figure 18. Pressure coefficient distribution using quartic approximation; on the left, reduced frequency is 1.0, on the right 2.0.

2.4.3 Rectangular wing, 20 chord wise boxes (box AR = 2.0).

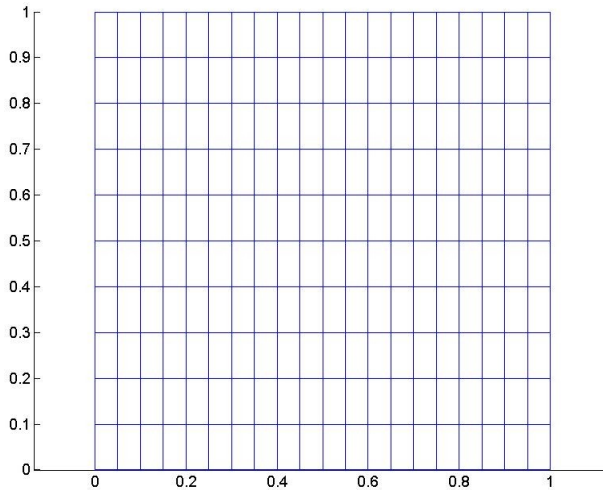


Figure 19. Rectangular wing, box AR = 2.0.

k	N5KQ		Quadratic approximation		Quartic approximation	
	real(CL)	imag(CL)	real(CL)	imag(CL)	real(CL)	imag(CL)
0.1	2.971	0.3563	2.9912	0.3792	2.9789	0.3688
0.5	3.859	1.712	3.9453	1.7793	3.9004	1.7467
1.0	4.901	1.313	4.9784	1.3133	4.9635	1.2760
2.0	5.720	1.393	5.7653	1.4133	5.7389	1.3474

Table 11. Total lift coefficient for a rectangular wing, box AR = 2.0.

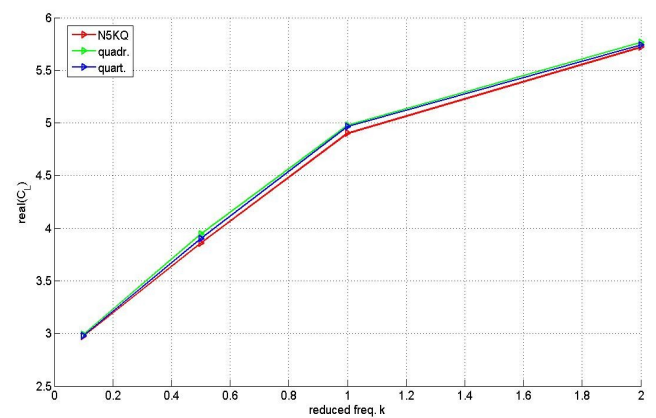
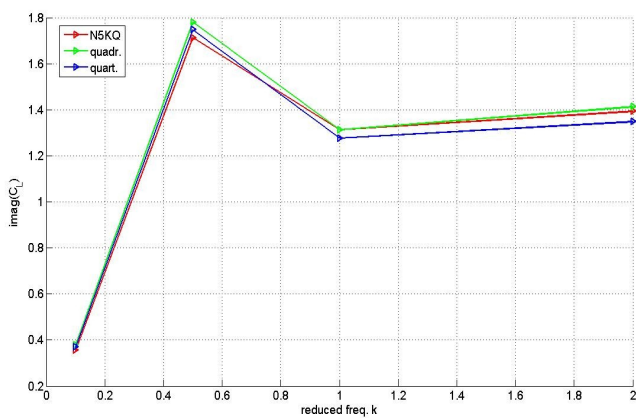


Figure 20. Real and imaginary part of the total lift coefficient, box AR = 2.0.

Lift Distributions on Planar and Non-Planar Configurations

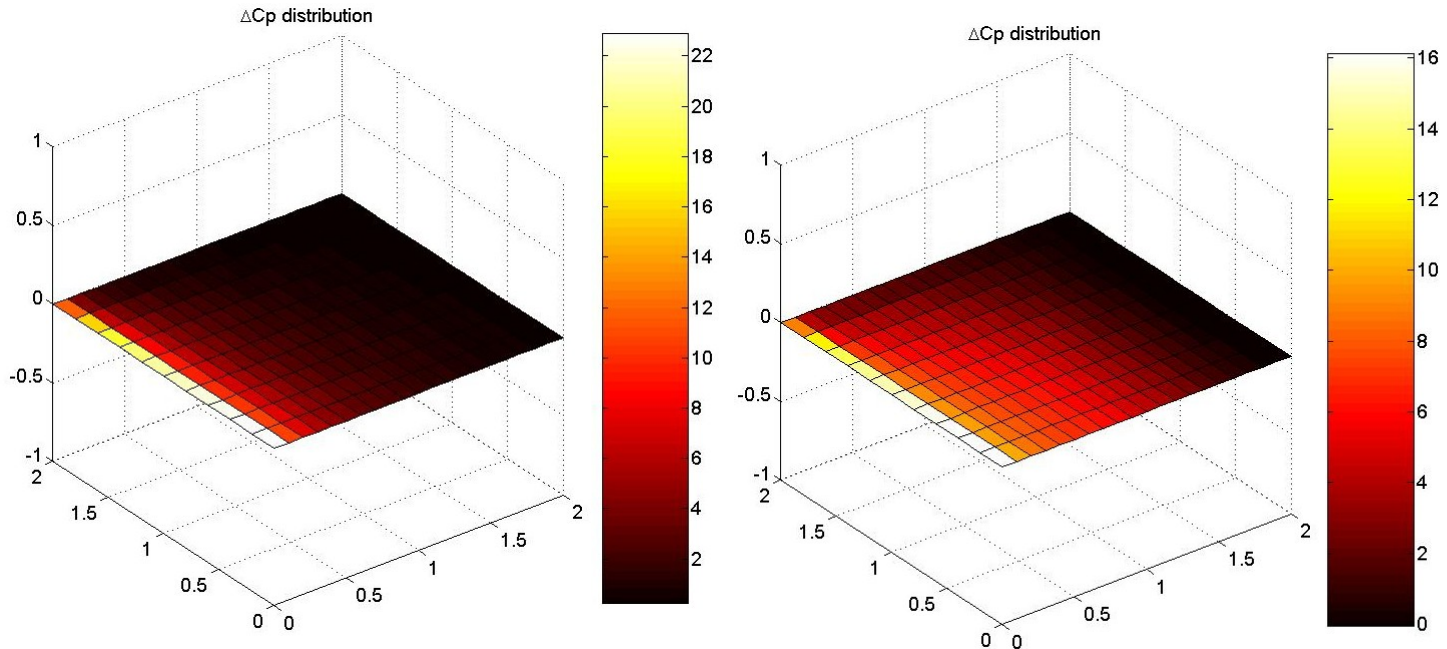


Figure 21. Pressure coefficient distribution using quartic approximation; on the left, reduced frequency is 0.1, on the right 0.5.

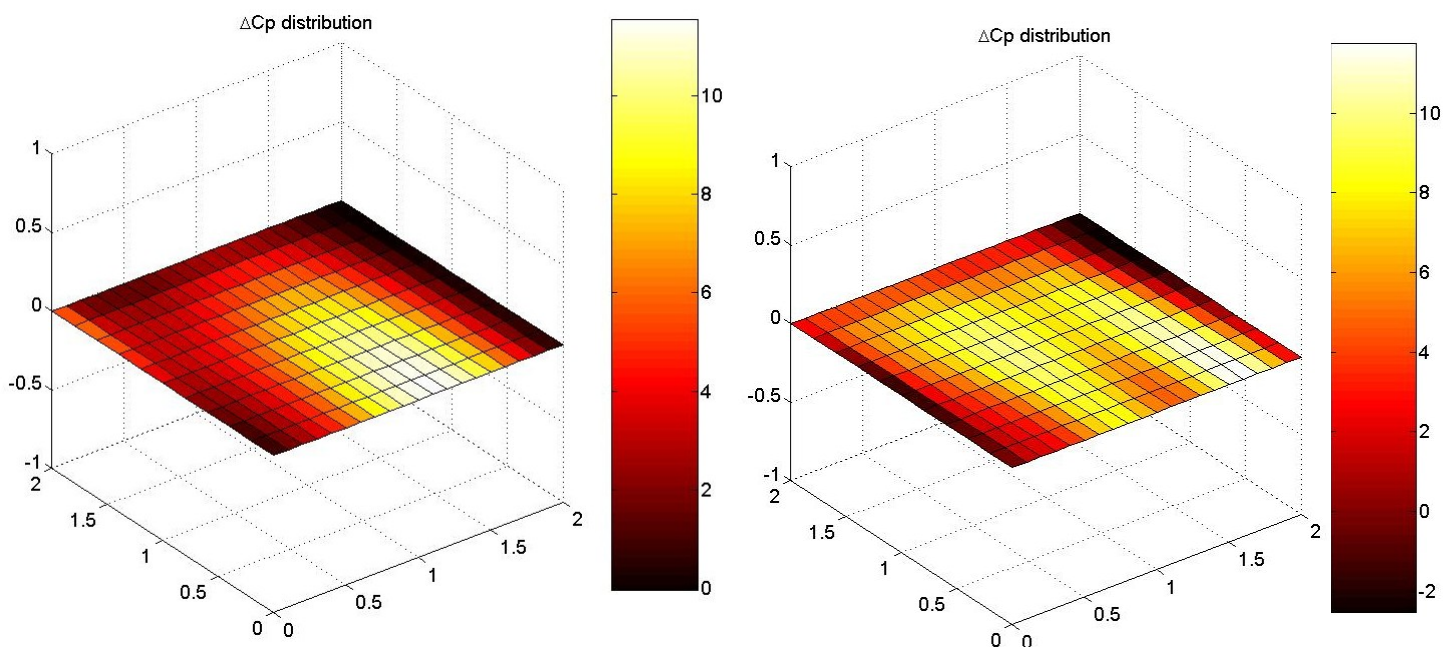


Figure 22. Pressure coefficient distribution using quartic approximation; on the left, reduced frequency is 1.0, on the right 2.0.

2.4.4 Rectangular wing, 50 chord wise boxes (box AR = 5.0)

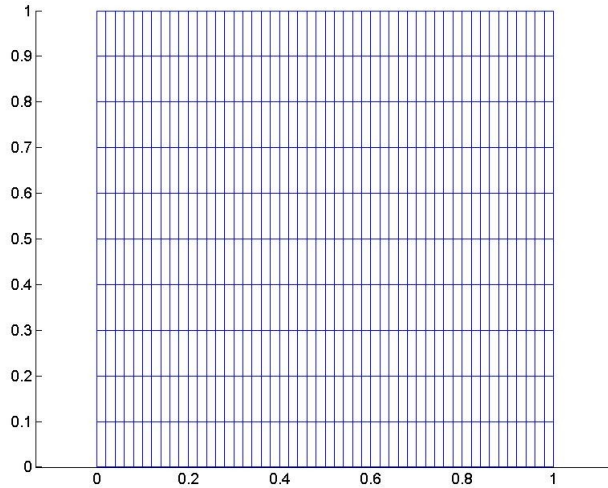


Figure 23. Rectangular wing, box AR = 5.0.

k	N5KQ		Quadratic approximation		Quartic approximation	
	real(CL)	imag(CL)	real(CL)	imag(CL)	real(CL)	imag(CL)
0.1	2.972	0.3560	3.0017	0.3912	2.9853	0.3739
0.5	3.898	1.706	4.0178	1.8268	3.9695	1.7635
1.0	4.948	1.212	5.0568	1.2843	5.0347	1.1655
2.0	5.840	1.194	5.9087	1.3324	5.8964	1.1393

Table 12. Total lift coefficient for a rectangular wing, box AR = 5.0.

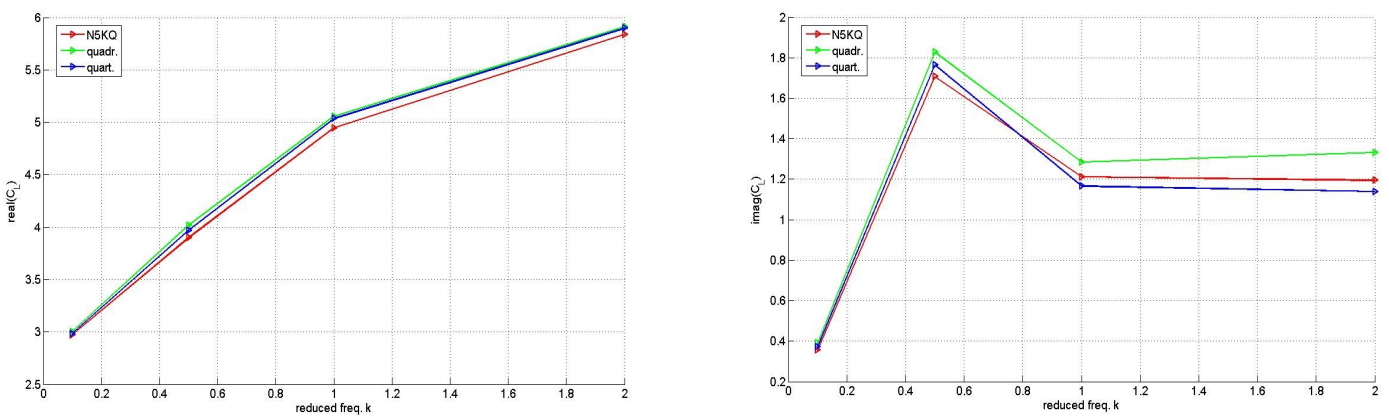


Figure 24. Real and imaginary part of the total lift coefficient, box AR = 5.0.

Lift Distributions on Planar and Non-Planar Configurations

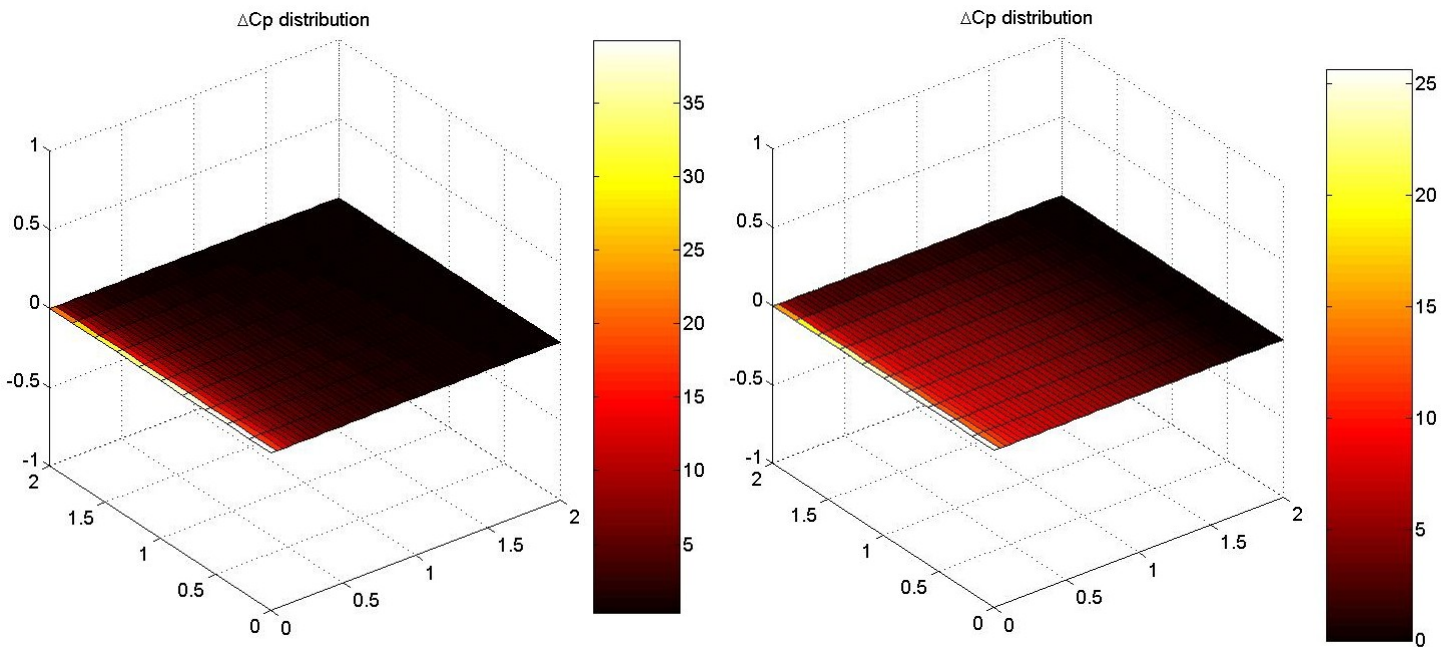


Figure 25. Pressure coefficient distribution using quartic approximation; on the left, reduced frequency is 0.1, on the right 0.5.

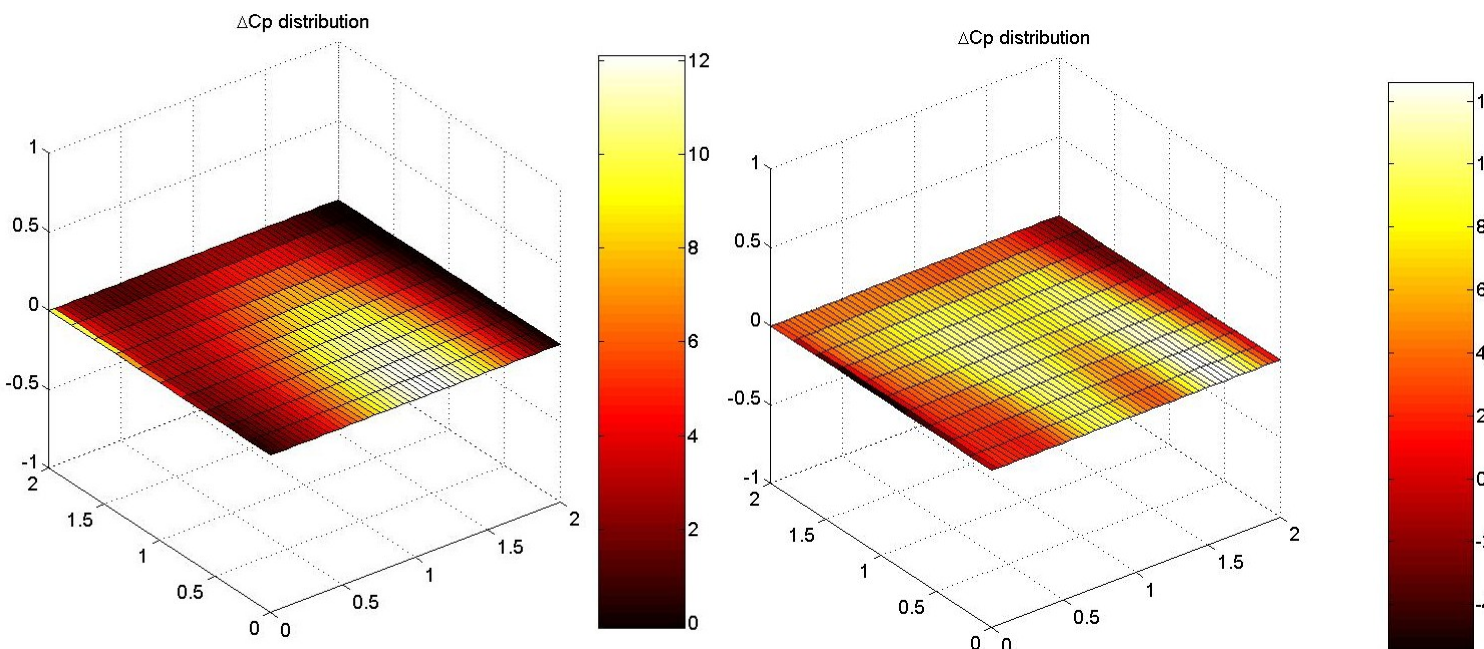


Figure 26. Pressure coefficient distribution using quartic approximation; on the left, reduced frequency is 1.0, on the right 2.0.

2.5 Rectangular wing, 20 equal-width strips, 20 equal-chord boxes, from Reference [8].

The second study of the box AR presented in the paper is on rectangular wing, now divided into 20 equal-width strips having 20 equal chord boxes. The box ARs are increased from 1.0 to 5.0 by an increase in the span so that the wing AR varies from 2.0 to 10.0. The same four reduced frequencies in **Table 8** are considered.

Only the right half wing is modeled and symmetry is used. All the results are shown in the following sections.

2.5.1 Rectangular AR = 2 wing, box AR = 1.0.

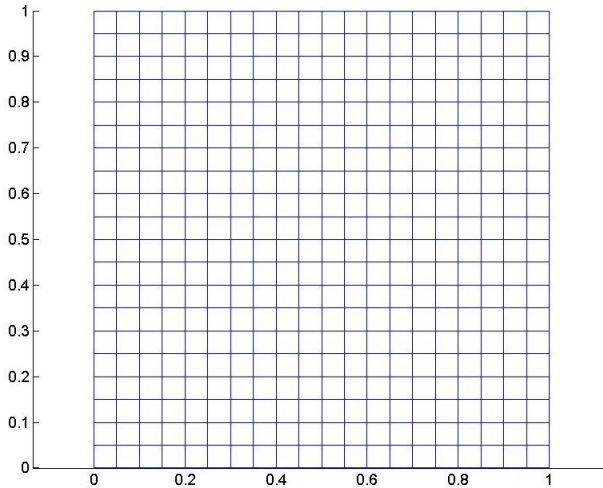


Figure 27. Rectangular AR = 2 wing, box AR = 1.0.

k	N5KQ		Quadratic approximation		Quartic approximation	
	real(CL)	imag(CL)	real(CL)	imag(CL)	real(CL)	imag(CL)
0.1	2.908	0.3546	2.9174	0.3680	2.9142	0.3662
0.5	3.775	1.709	3.8290	1.7461	3.8034	1.7482
1.0	4.832	1.335	4.9112	1.2855	4.9045	1.3215
2.0	5.610	1.432	5.6633	1.3473	5.6440	1.4054

Table 13. Total lift coefficient for rectangular AR = 2 wing, box AR = 1.0.

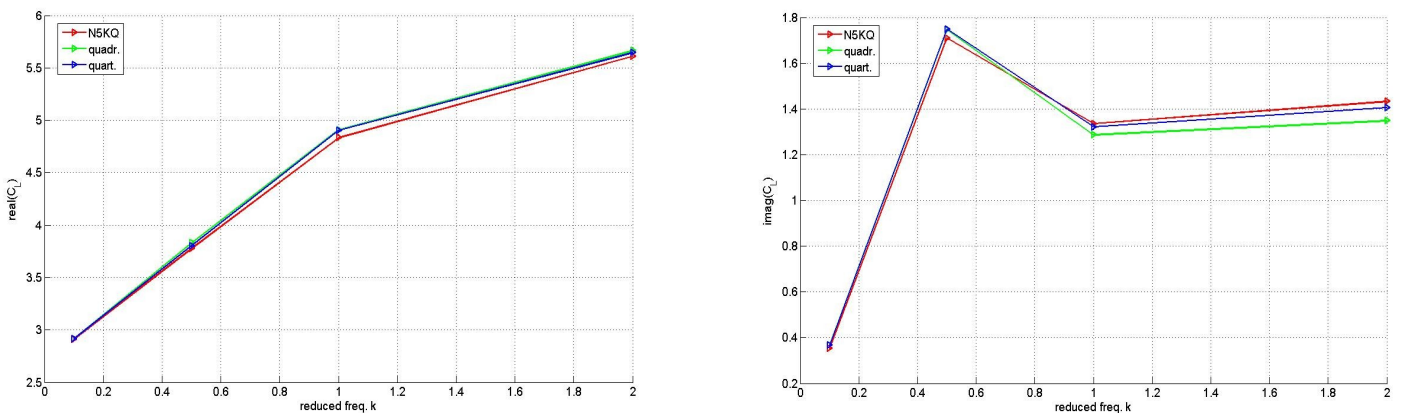


Figure 28. Real and imaginary part of the total lift coefficient, wing AR = 2 and box AR = 1.0.

Lift Distributions on Planar and Non-Planar Configurations

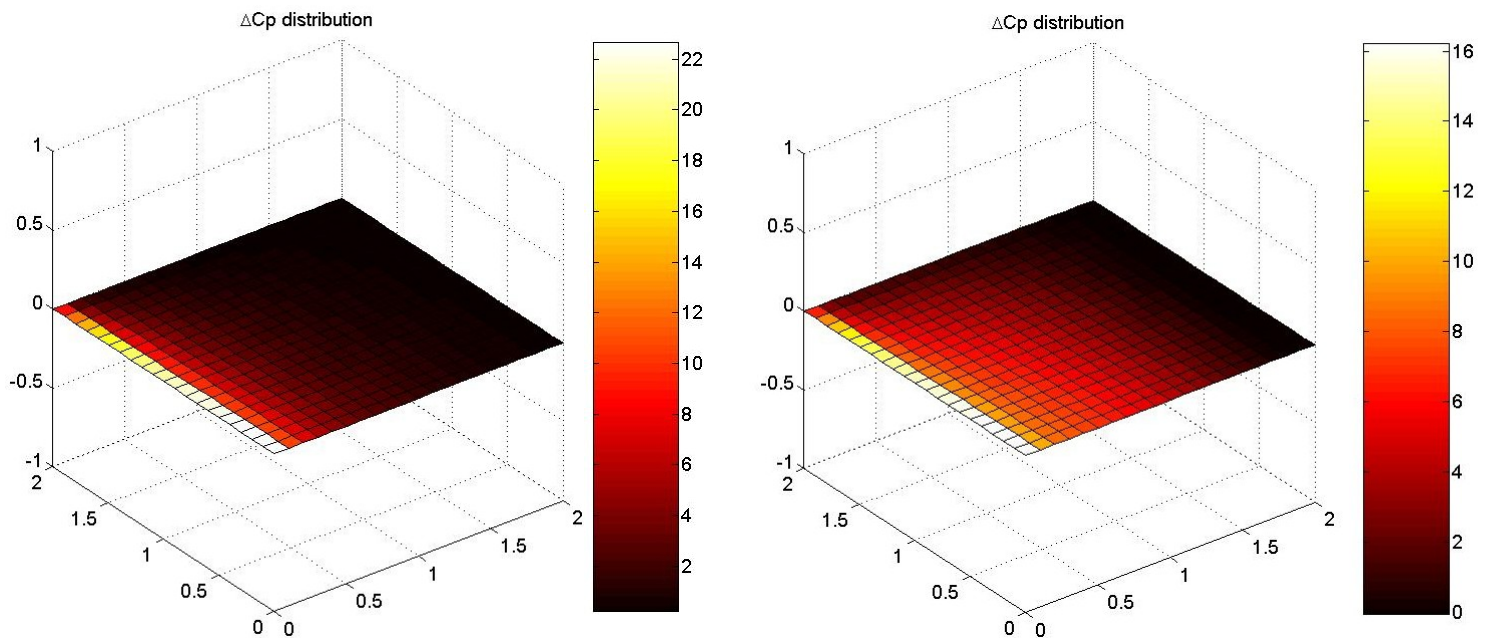


Figure 29. Pressure coefficient distribution using quartic approximation; on the left, reduced frequency is 0.1, on the right 0.5.

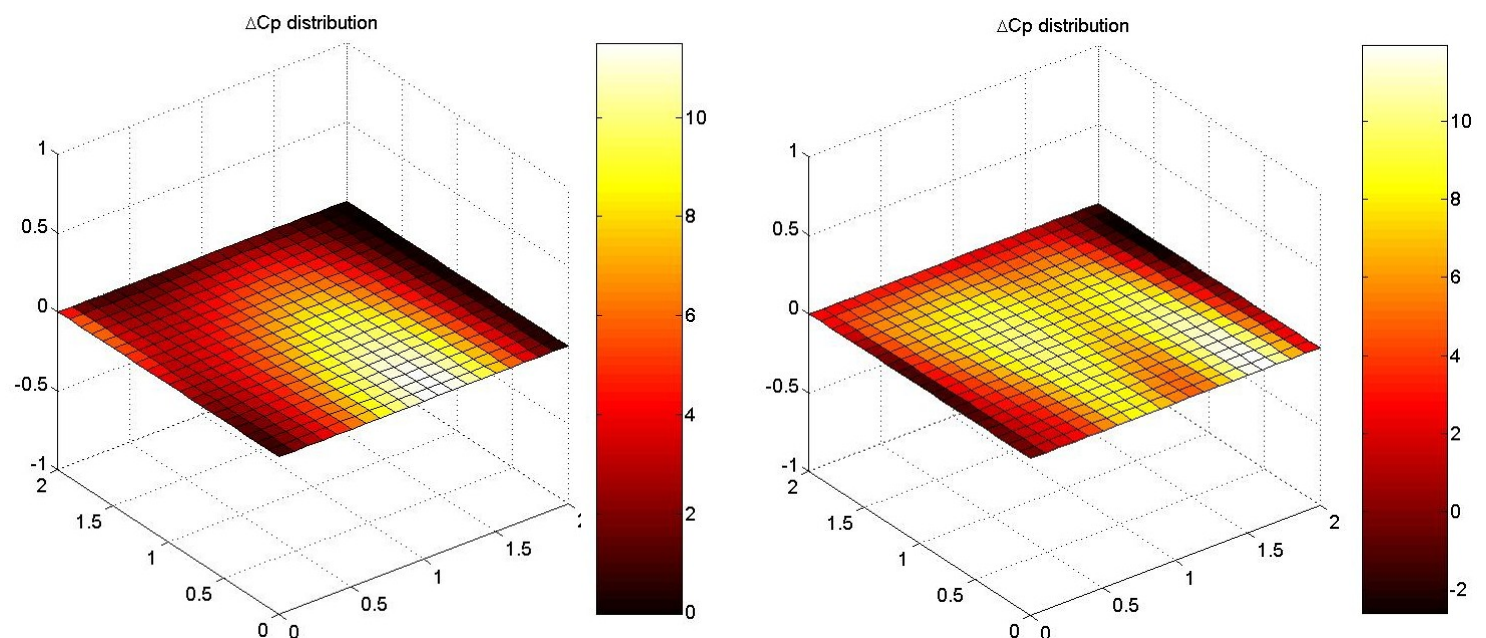


Figure 30. Pressure coefficient distribution using quartic approximation; on the left, reduced frequency is 1.0, on the right 2.0.

2.5.2 Rectangular AR = 4 wing, box AR = 2.0.

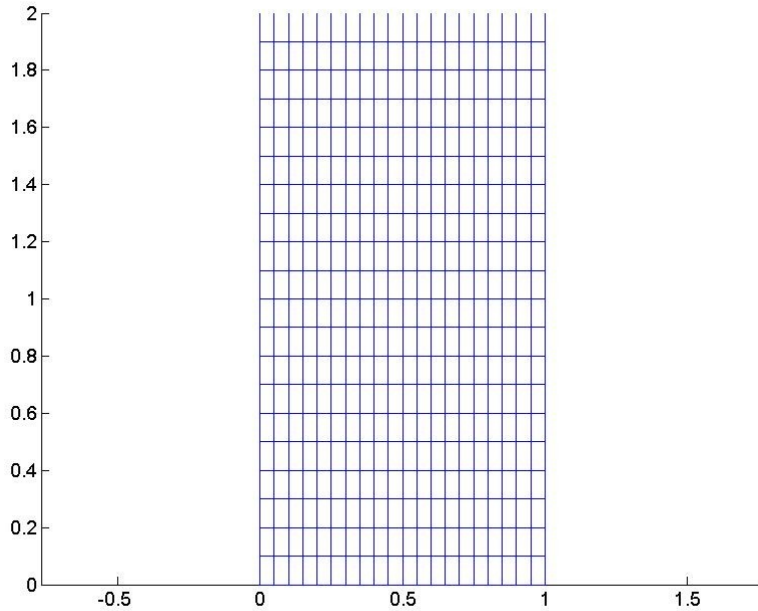


Figure 31. Rectangular AR = 4 wing, box AR = 2.0.

N5KQ			Quadratic approximation		Quartic approximation	
k	real(CL)	imag(CL)	real(CL)	imag(CL)	real(CL)	imag(CL)
0.1	4.587	-0.0370	4.6511	-0.0051	4.6132	-0.0136
0.5	4.701	0.5339	4.8290	0.5361	4.7714	0.5353
1.0	4.874	0.9398	4.9508	0.9411	4.9227	0.9038
2.0	5.800	0.9705	5.8484	0.9853	5.8112	0.9211

Table 14. Total lift coefficient for rectangular AR = 4 wing, box AR = 2.0.

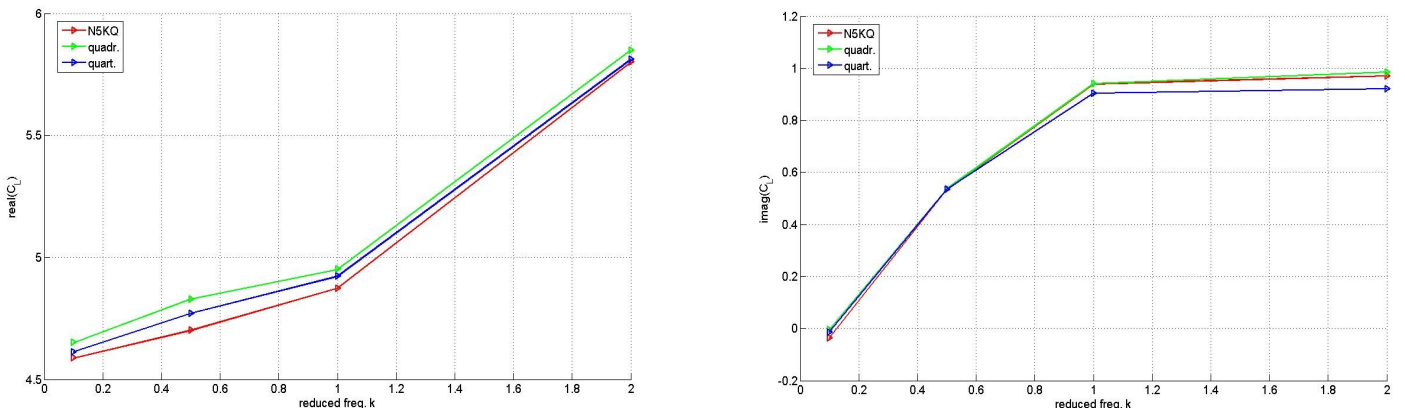


Figure 32. Real and imaginary part of lift coefficient, wing AR = 4 and box AR = 2.0.

Lift Distributions on Planar and Non-Planar Configurations

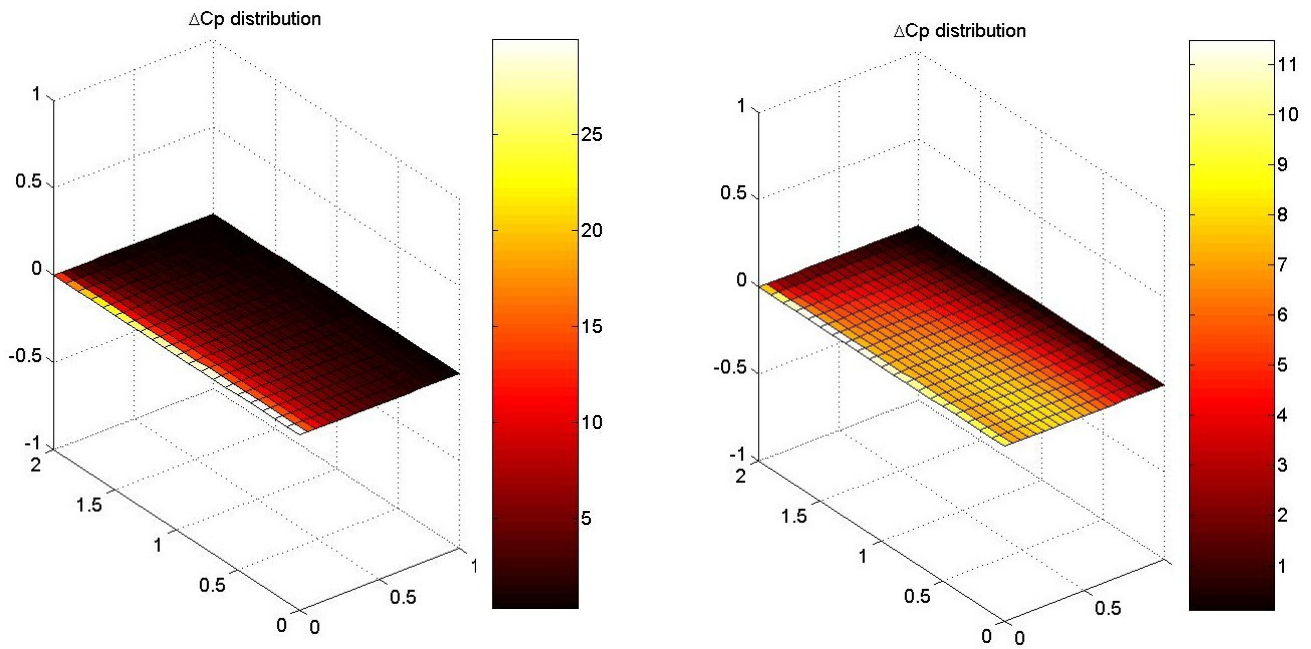


Figure 33. Pressure coefficient distribution using quartic approximation; on the left, reduced frequency is 0.1, on the right 0.5.

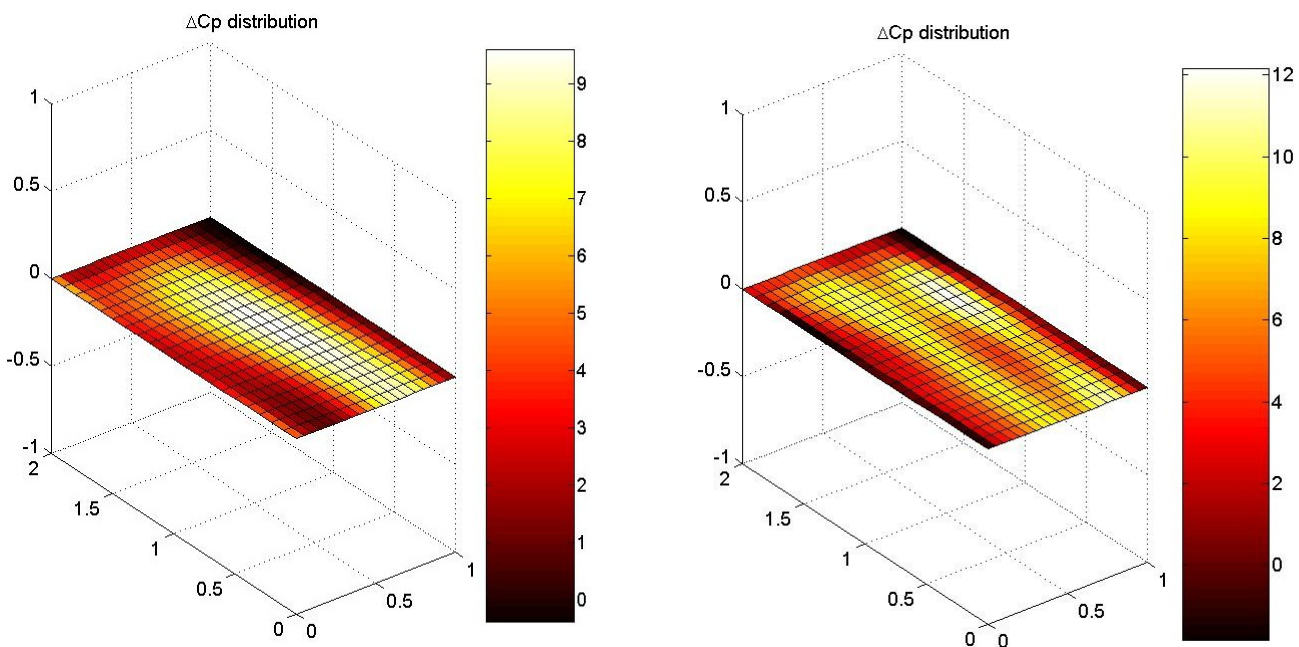


Figure 34. Pressure coefficient distribution using quartic approximation; on the left, reduced frequency is 1.0, on the right 2.0.

2.5.3 Rectangular AR = 6 wing, box AR = 3.0.

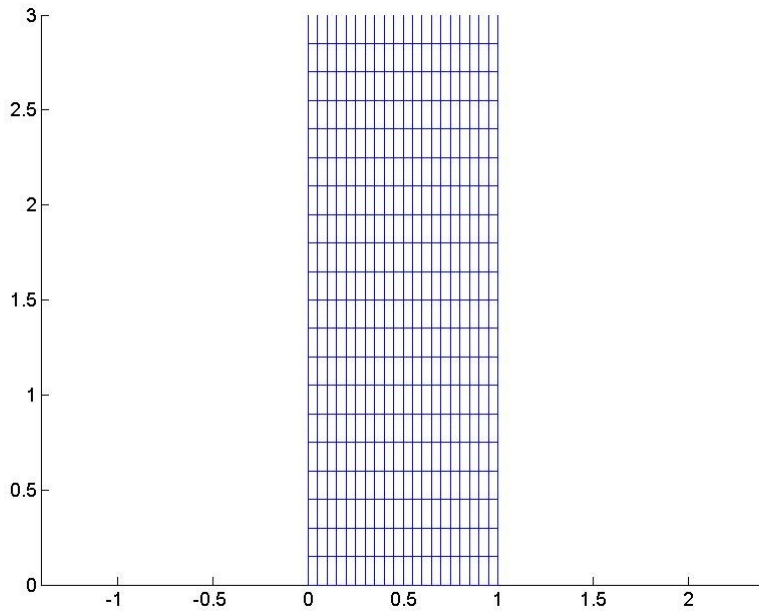


Figure 35. Rectangular AR = 6 wing, box AR = 3.0.

k	N5KQ		Quadratic approximation		Quartic approximation	
	real(CL)	imag(CL)	real(CL)	imag(CL)	real(CL)	imag(CL)
0.1	5.414	-0.5164	5.5666	-0.4881	5.4674	-0.4933
0.5	4.747	0.2547	4.9213	0.2663	4.8258	0.2348
1.0	4.921	0.7556	5.0330	0.8342	4.9615	0.7077
2.0	5.856	0.8407	5.9309	0.9957	5.8578	0.7896

Table 15. Total lift coefficient for rectangular AR = 6 wing, box AR = 3.0.

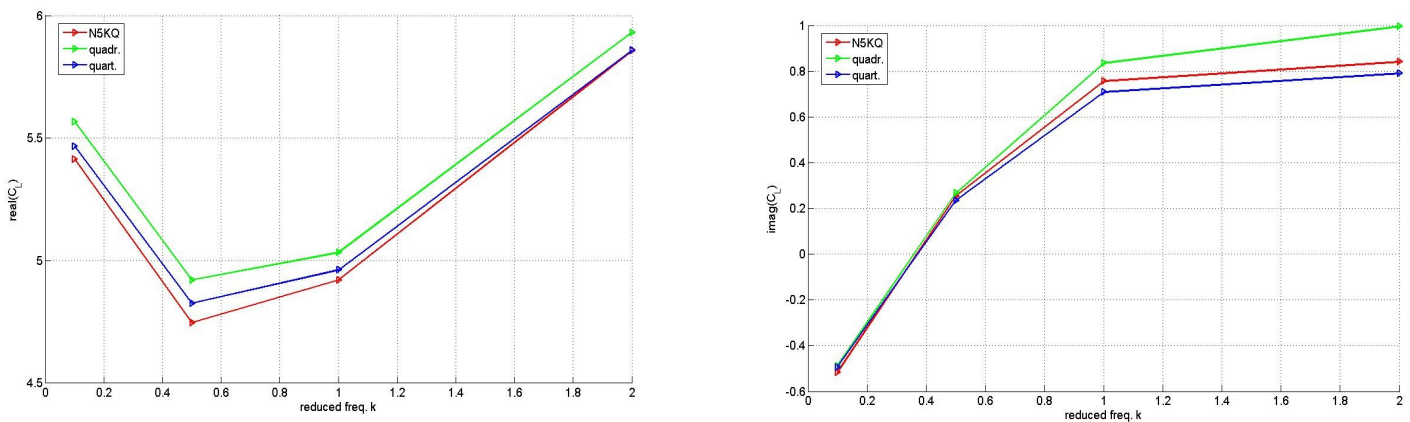


Figure 36. Real and imaginary part of lift coefficient, wing AR = 6 and box AR = 3.0.

Lift Distributions on Planar and Non-Planar Configurations

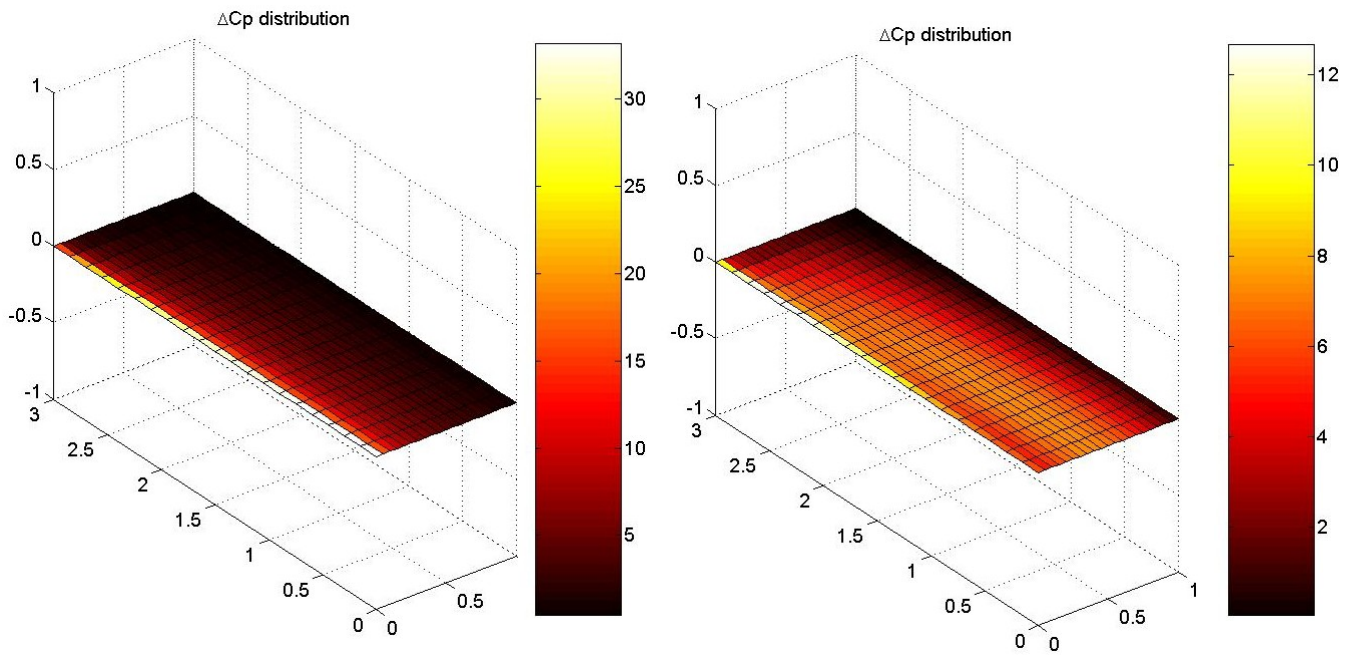


Figure 37. Pressure coefficient distribution using quartic approximation; on the left, reduced frequency is 0.1, on the right 0.5.

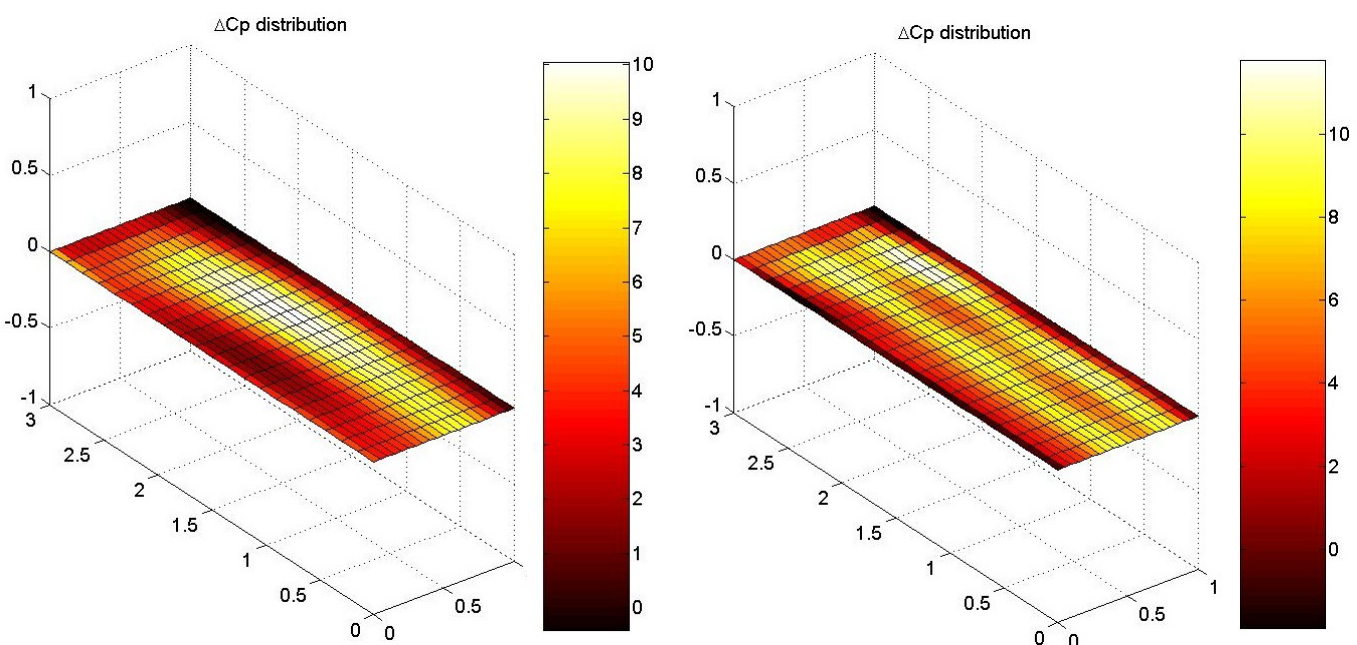


Figure 38. Pressure coefficient distribution using quartic approximation; on the left, reduced frequency is 1.0, on the right 2.0.

2.5.4 Rectangular AR = 10 wing, box AR = 5.0.

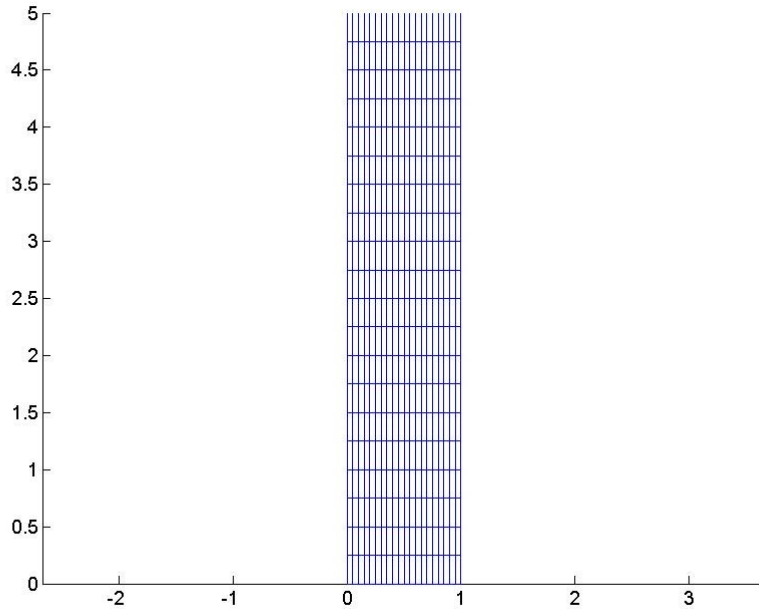


Figure 39. Rectangular AR = 10 wing, box AR = 5.0.

k	N5KQ		Quadratic approximation		Quartic approximation	
	real(CL)	imag(CL)	real(CL)	imag(CL)	real(CL)	imag(CL)
0.1	6.038	-1.166	6.3735	-1.1947	6.1590	-1.1696
0.5	4.873	0.0507	5.1769	0.0953	4.9995	0.0036
1.0	4.989	0.6529	5.2104	0.8731	5.0476	0.5995
2.0	5.878	0.8073	5.9950	1.1909	5.9240	0.7541

Table 16. Total lift coefficient for rectangular AR = 10 wing, box AR = 5.0.

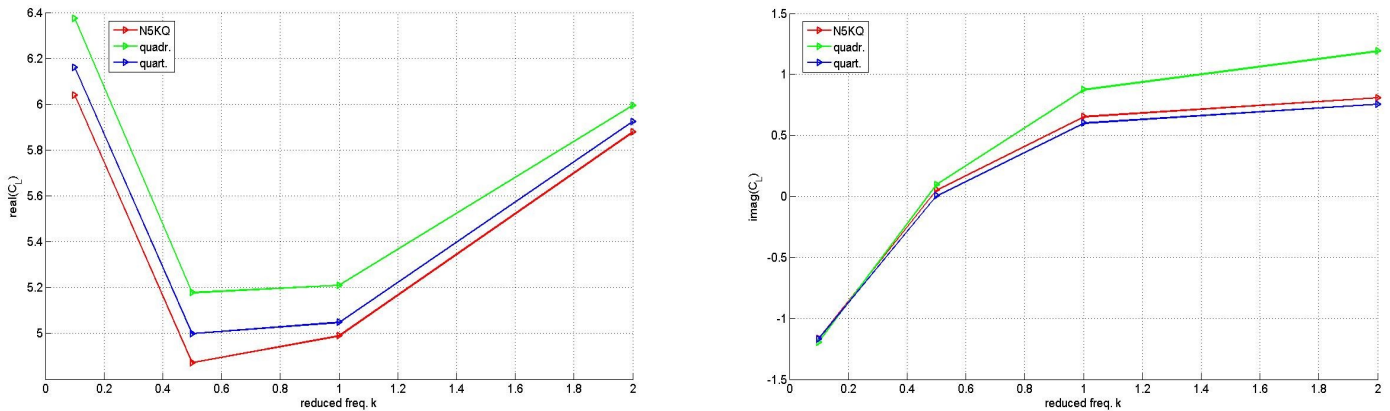


Figure 40. Real and imaginary part of lift coefficient, wing AR = 10 and box AR = 5.0.

Lift Distributions on Planar and Non-Planar Configurations

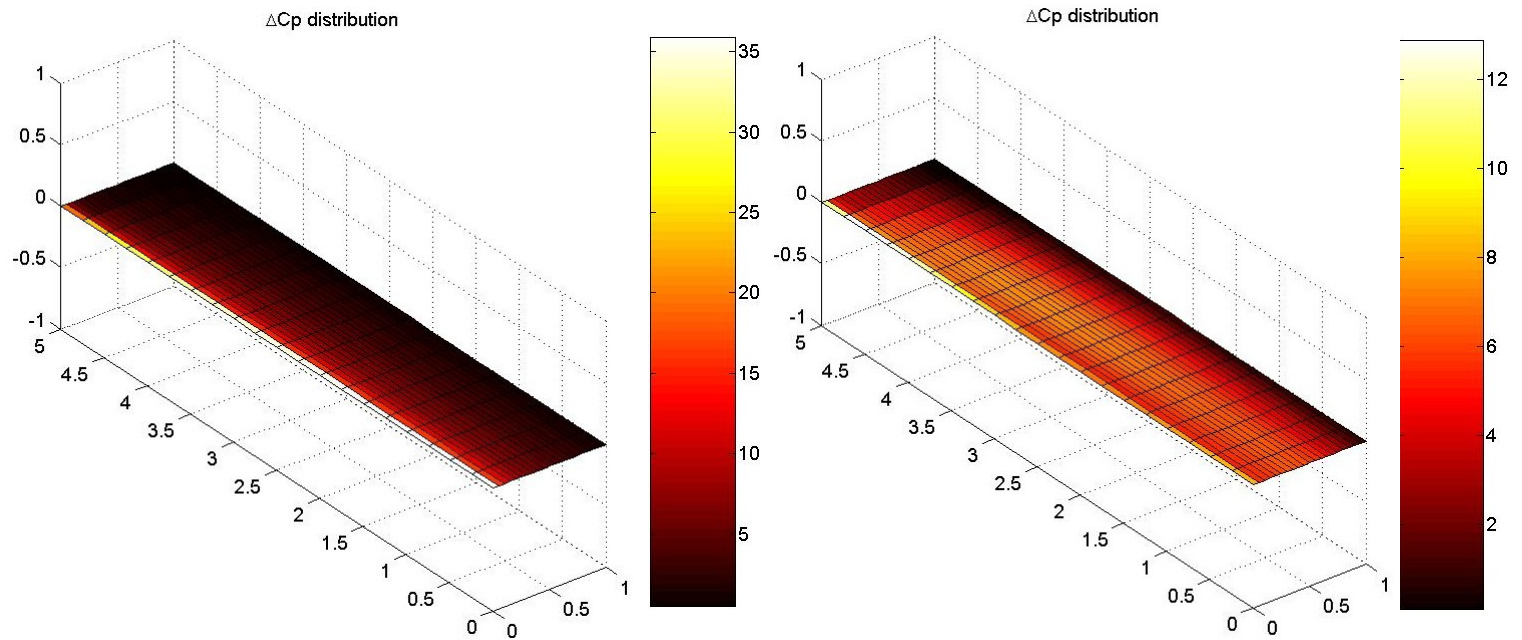


Figure 41. Pressure coefficient distribution using quartic approximation; on the left, reduced frequency is 0.1, on the right 0.5.

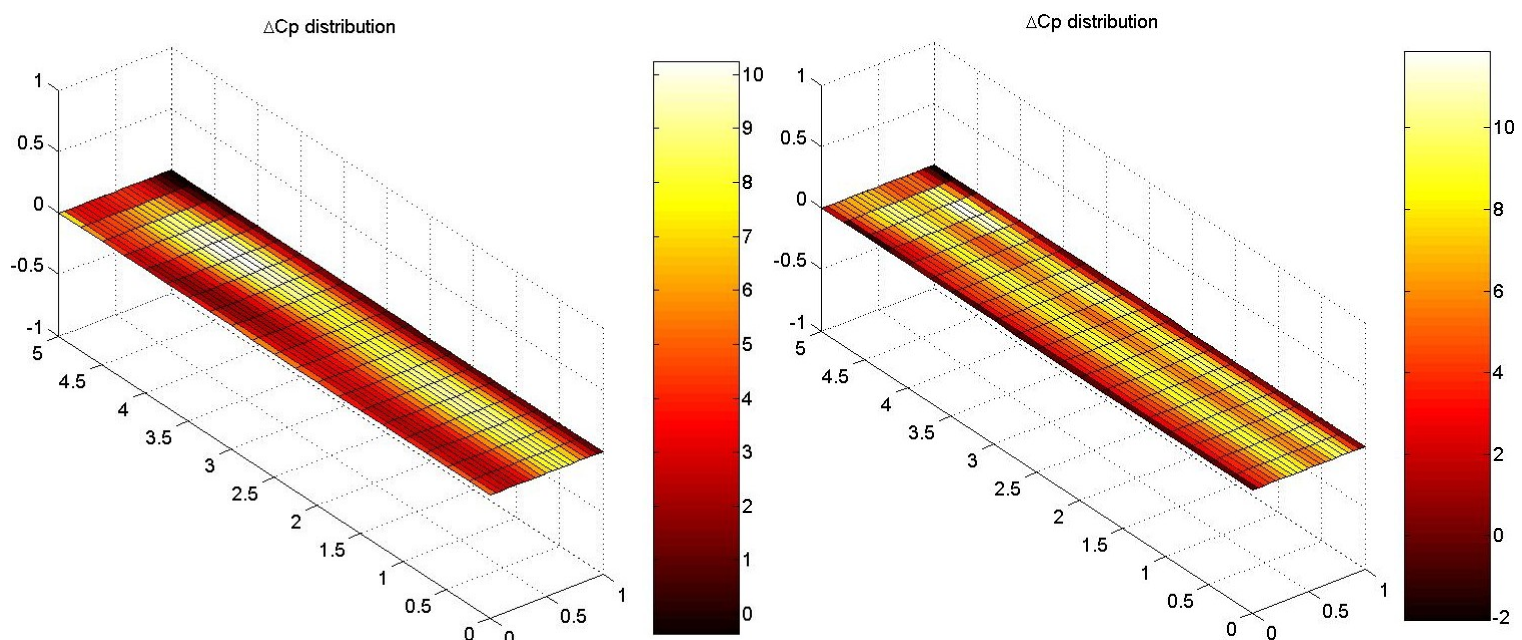


Figure 42. Pressure coefficient distribution using quartic approximation; on the left, reduced frequency is 1.0, on the right 2.0.

2.6 FSW airplane in level flight,

from Reference [19], *Example HA144A*.

The FSW airplane is shown in **Figure 43**. The wing has an aspect ratio of 4.0, no taper, twist, or camber, but an incidence of 0.1 deg relative to the fuselage, and a forward sweep angle of 30 deg. The canard has an aspect ratio of 1.0, no taper, twist, camber, incidence or sweep. The chords of both the wing and canard are 10.0 ft, the reference chord is chosen as 10 ft and the reference area is 200 sq ft for the half span model. A subsonic speed ($M = 0.9$) is considered.

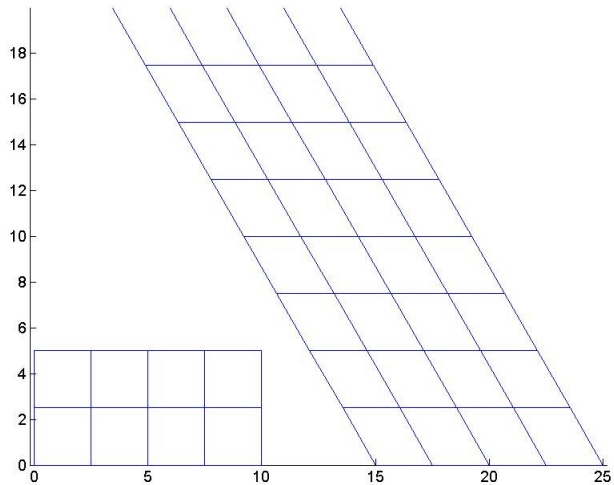


Figure 43. FSW airplane: non-planar configuration.

The subsonic derivative $C_{L,\alpha}$ is computed and results from simulations are compared with NASTRAN output. Results are reported in **Table 17**. Pressure coefficient distribution for quartic approximation is shown in **Figure 44**.

	NASTRAN	Quadratic approximation	Quartic approximation
$C_{L,\alpha}$	5.071	5.0042	5.0699

Table 17. Subsonic derivative for FSW airplane.

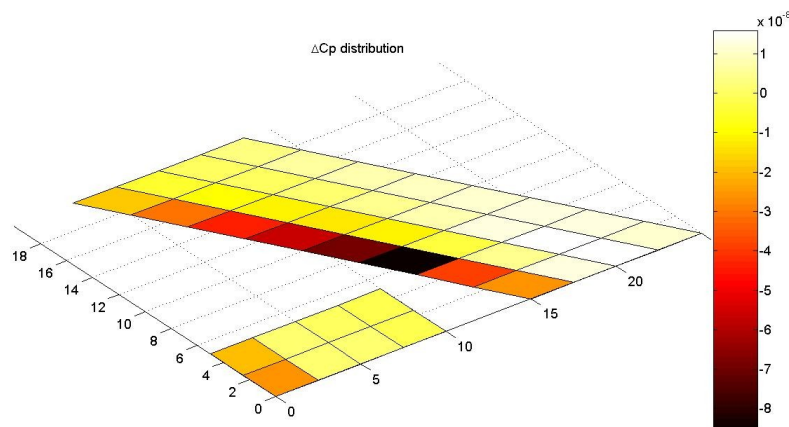


Figure 44. Pressure coefficient distribution using quartic approximation.

2.7 FSW airplane in antisymmetric maneuvres,

from Reference [19], *Example HA144D.*

The FSW airplane considered in the above section is modified and the lateral-directional derivative is computed. A 30 deg sweepback fin is added. It has no taper, a chord and a span of 10 ft. The half span model is shown in **Figure 45**.

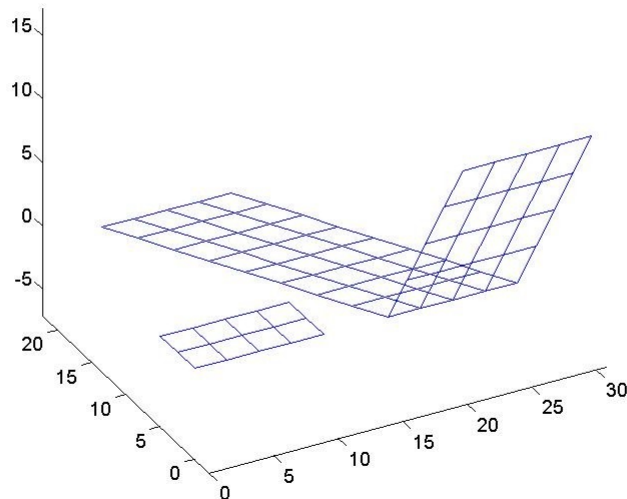


Figure 45. FSW airplane with a sweptback fin.

The subsonic derivative $C_{Y,\beta}$, as defined in equation 15 at page 13, is computed for a unitary side motion along y-axis from the complex aerodynamic side force and results are compared with NASTRAN output. They are reported in **Table 18**.

NASTRAN		Quadratic approximation		Quartic approximation		
k	real(F _y)	imag(F _y)	real(F _y)	imag(F _y)	real(F _y)	imag(F _y)
0.001	1.2752e-005	-2.8634e-002	2.3993e-005	-2.4246e-002	2.8479e-005	-2.3883e-002
0.01	1.2748e-003	-2.8634e-001	2.4100e-003	-2.4246e-001	2.8465e-003	-2.3884e-001
NASTRAN		Quadratic approximation		Quartic approximation		
k	$C_{Y,\beta}$		$C_{Y,\beta}$		$C_{Y,\beta}$	
0.001	0.7158		0.6061		0.5970	
0.01	0.7158		0.6061		0.5971	

Table 18. Subsonic complex aerodynamic lateral force and lateral-directional derivative for FSW airplane.

2.8 Generalized Influence Matrix

Further, the computer program is used to calculate the generalized aerodynamic influence coefficient (AIC) matrix for the AGARD wing 445.6, already described in **Section 2.3** and in Reference [19]. The calculations are performed for 2 different Mach number, $M = 0.678$ and $M = 0.96$, and several values of reduced frequency, as shown in the following figures. It must be remarked the latter flight condition is transonic and thus the adoption of the Doublet Lattice Method is a wrong and dangerous choice. The adoption of a linearized potential theory neglects non-linear phenomena associated to viscosity and compressibility which can result in over-predicted flutter dynamic pressures (the so-called transonic dip phenomenon). The AIC matrix is here reported as a mere source of comparison of the present method. For this condition the aerodynamic system needs to be modeled through more complex theories based on Euler or Navier-Stokes equations.

The structural modes here considered are the first bending and first torsion mode, at frequencies of 14.1Hz and 50.9Hz , respectively. See **Figure 46.** for a graphical representation of these modes.

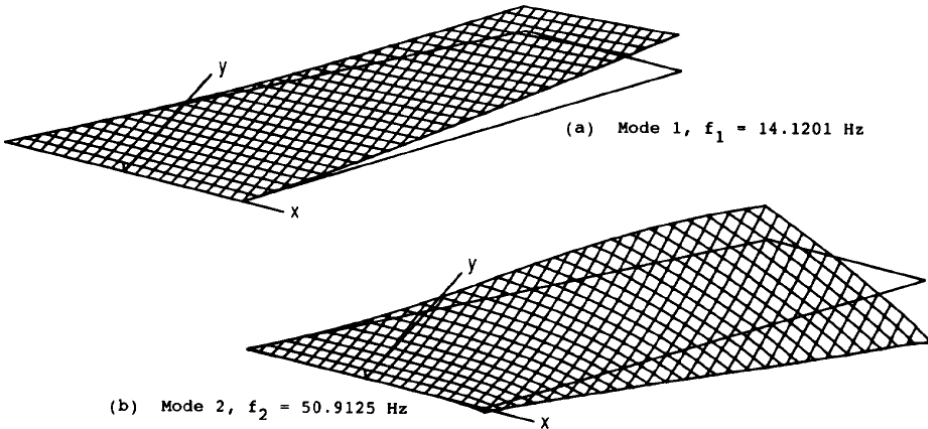


Figure 46. First bending and first torsion mode for AGARD 445.6 wing; 14.1Hz and 50.9Hz , respectively .

The values of the AIC matrix in the subsonic regime, $M = 0.678$, are reported in the Figure 47 - 50; the transonic simulations, $M = 0.96$, are instead shown in the Figure 51 - 54. Again, both approximations, quadratic and quartic, are used to evaluate numerically the numerator of the kernel function.

A delicate question regards the methods used for the spatial coupling among different discretizations. In aeroelasticity it is a common practice to use different discretization for aerodynamic and structural system. As a matter of fact these models need to transfer data such as displacements, velocities and forces. The algorithm used in the present method is different from the one used in N5KQ which adopts a simple surface-spline. The method used here is based on a Moving Least Square technique which enforces the conservation of the energy exchange between the two different discretizations. This is a delicate question in aeroelasticity because the spatial coupling procedure may numerically alter the stability of the system though a spurious introduction/loss of energy if not treated in the proper way. Further details regarding the present method can be found in Quaranta et al. [21].

The generalized AIC matrix is defined in the discretized form

$$Q_{ik} = \sum_{r=1}^{NP} w_{ri} \Delta p_{rk} S_r ,$$

as the sum over the number of boxes (NP) of the pressure coefficient difference due to the k -th mode times the box surface times the box displacement due to the i -th mode. Moreover, the boundary conditions have been imposed using the following relation

$$\alpha = \frac{\dot{w}}{U} + \frac{dw}{dx} = ik \frac{w}{c_r} + \frac{dw}{dx} .$$

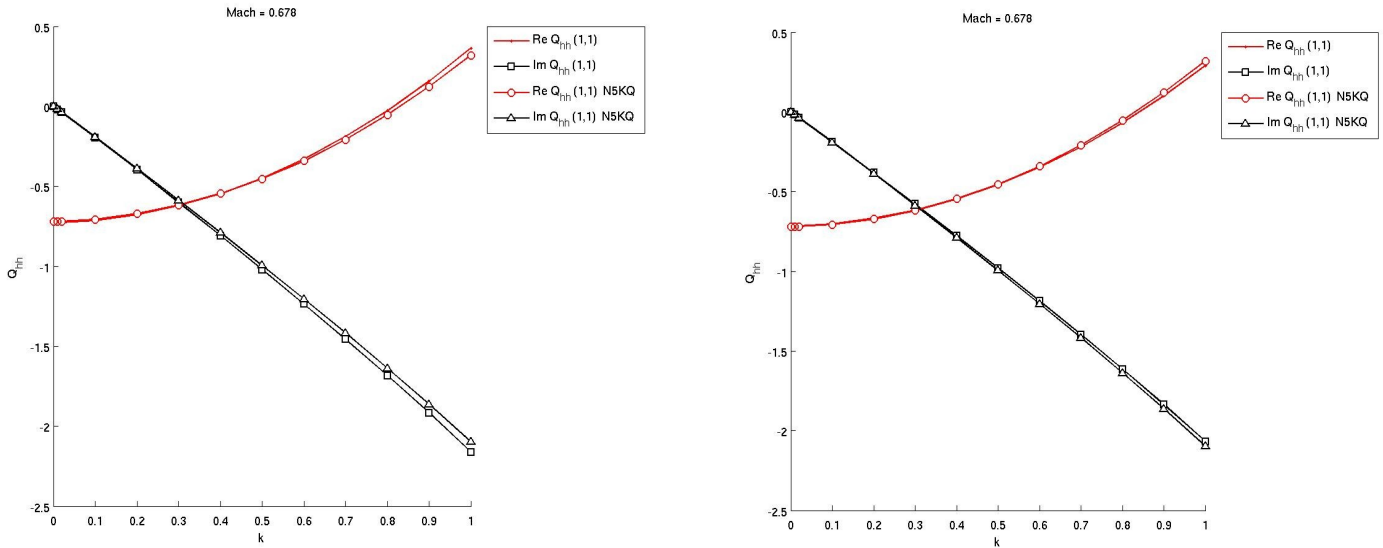


Figure 47. Q_{11} with quadratic (left) and quartic (right) approximation, $M = 0.678$.

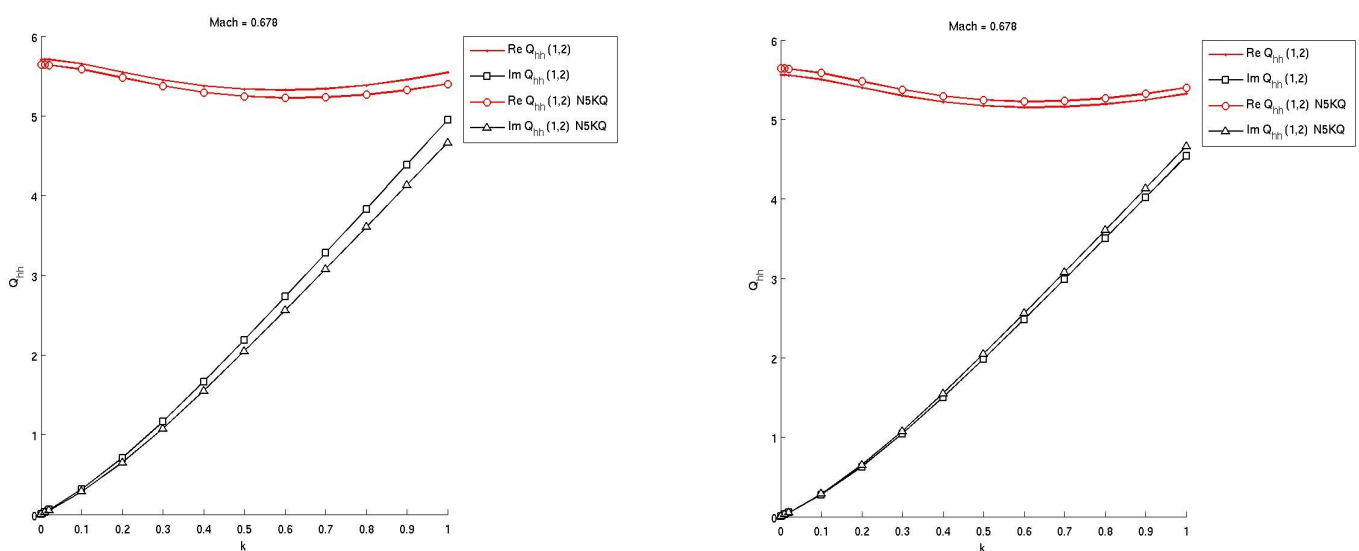


Figure 48. Q_{12} with quadratic (left) and quartic (right) approximation, $M = 0.678$.

Lift Distributions on Planar and Non-Planar Configurations

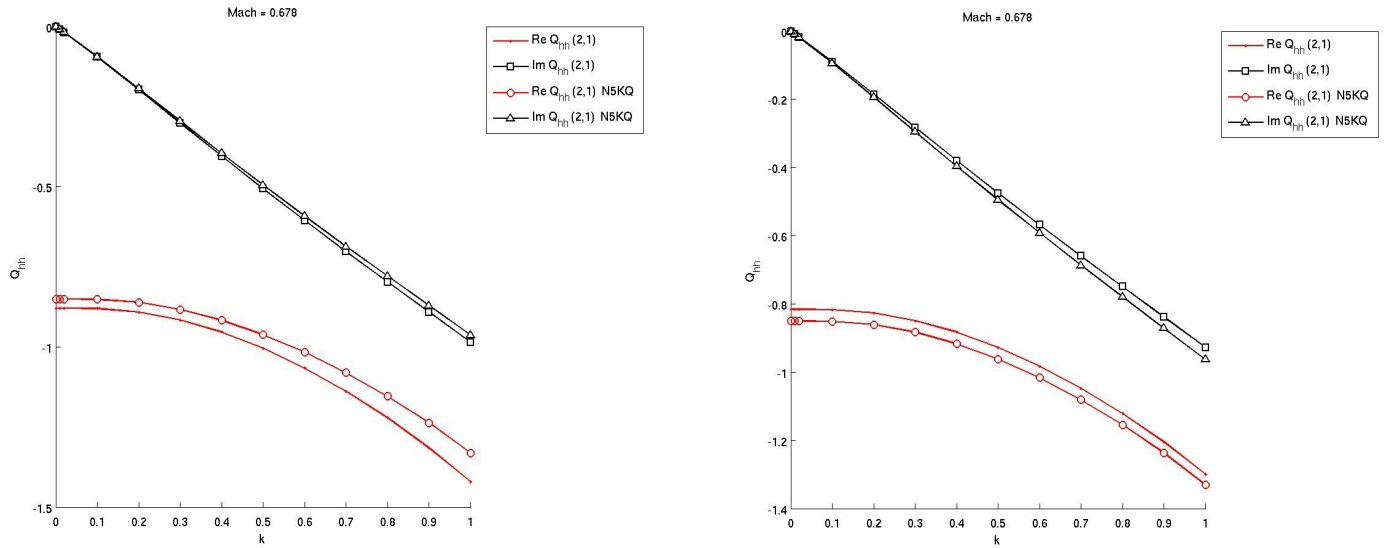


Figure 49. Q_{21} with quadratic (left) and quartic (right) approximation, $M = 0.678$.

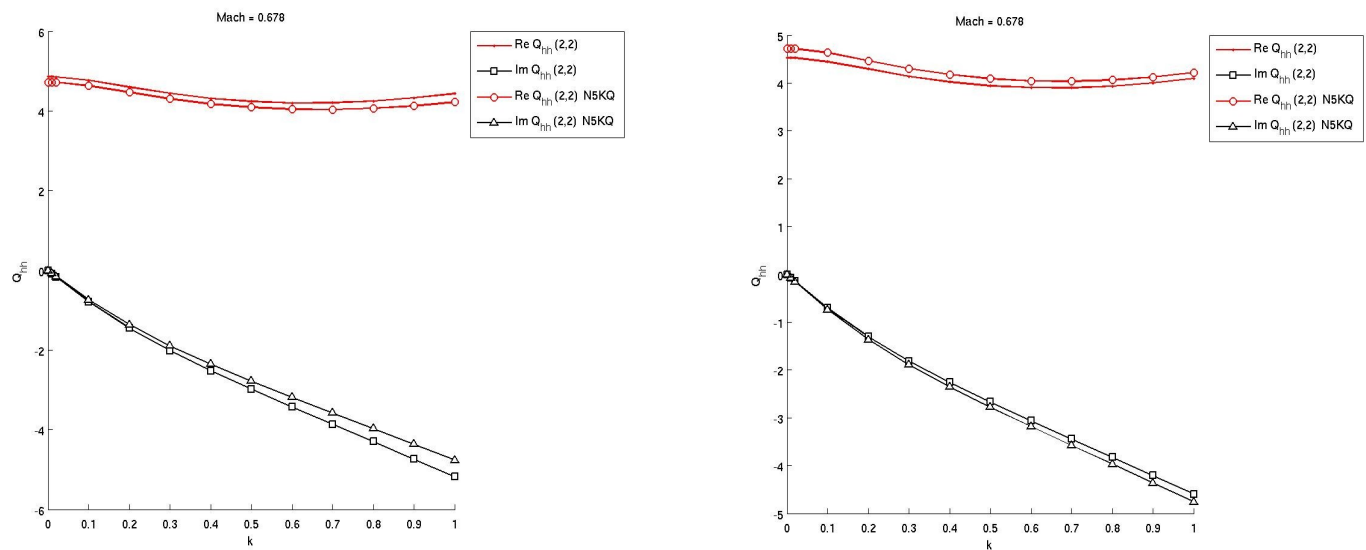


Figure 50. Q_{22} with quadratic (left) and quartic (right) approximation, $M = 0.678$.

Lift Distributions on Planar and Non-Planar Configurations

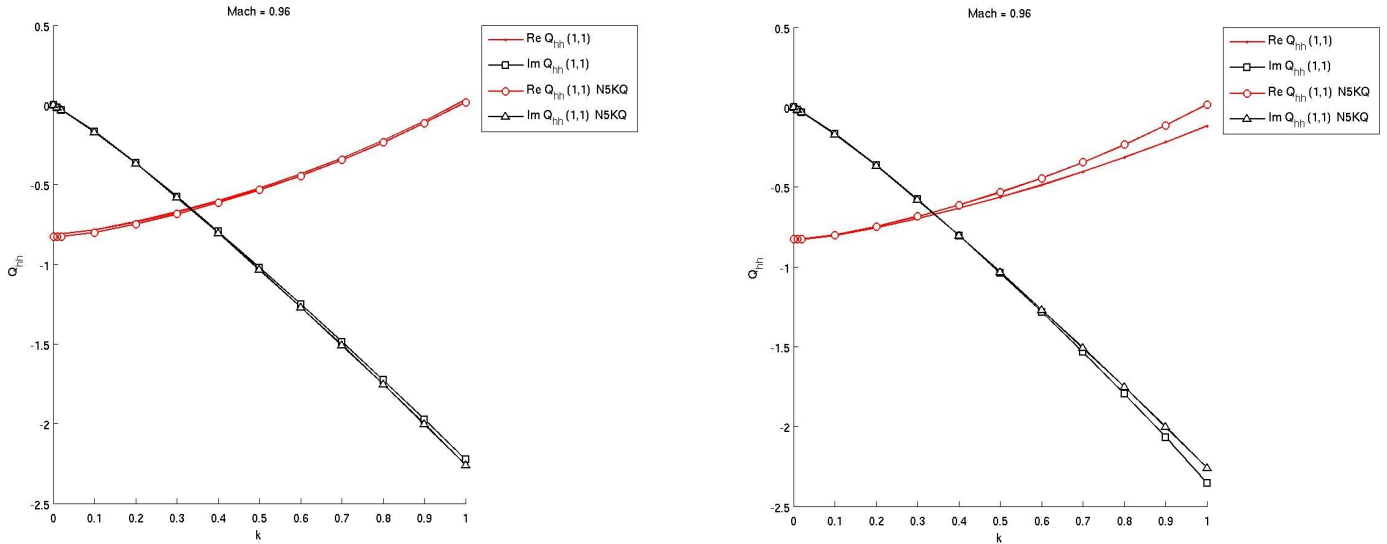


Figure 51. Q_{11} with quadratic (left) and quartic (right) approximation, $M = 0.96$.

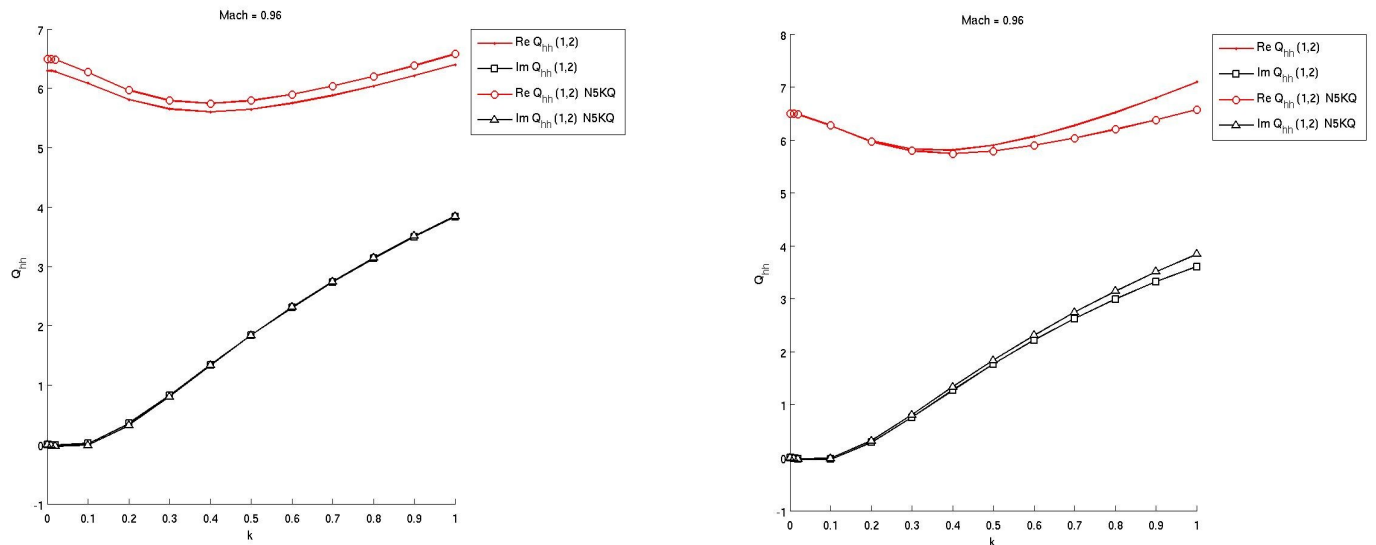


Figure 52. Q_{12} with quadratic (left) and quartic (right) approximation, $M = 0.96$.

Lift Distributions on Planar and Non-Planar Configurations

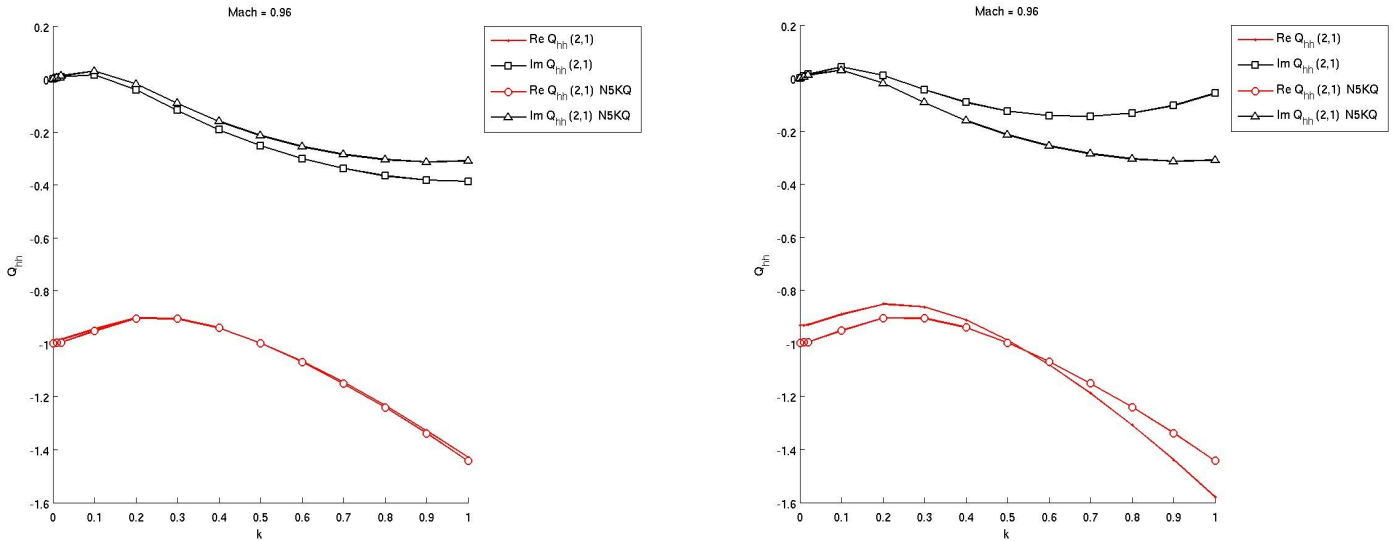


Figure 53. Q_{21} with quadratic (left) and quartic (right) approximation, $M = 0.96$.

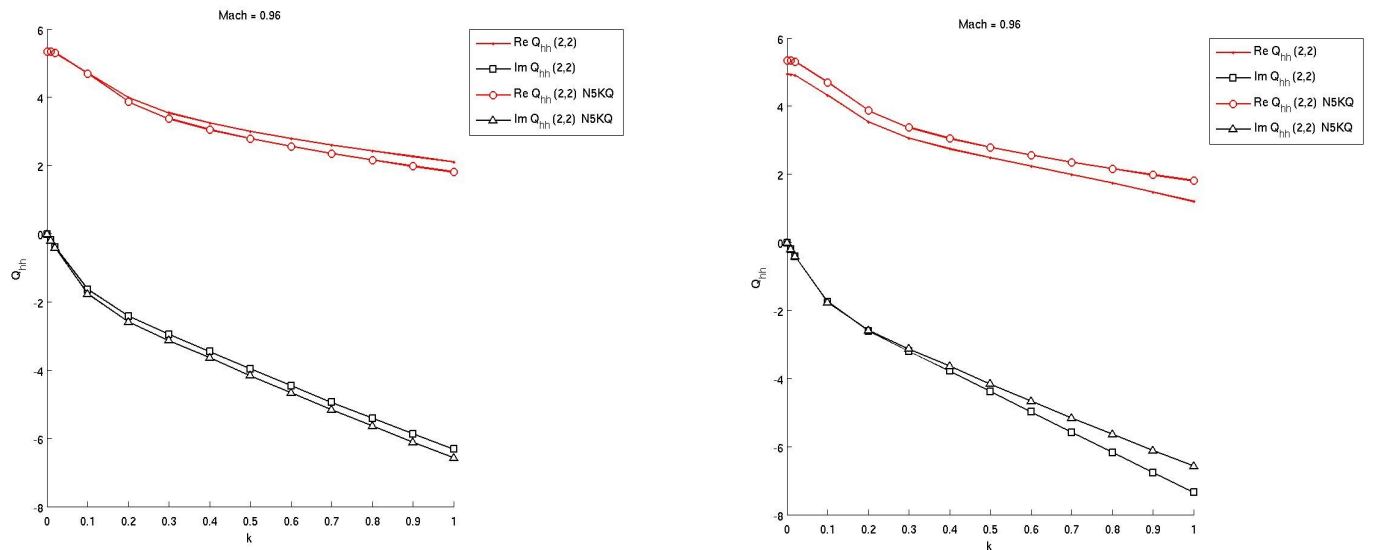


Figure 54. Q_{22} with quadratic (left) and quartic (right) approximation, $M = 0.96$.

3 Conclusions

Because the problem size depends on the number of elements used in the lifting-surfaces discretization, it is very important to use the minimum number of boxes which will provide accurate results. The introduction of the quartic approximation, although it is slightly more expansive than the quadratic due to the fact of the 5 evaluation points instead of 3, seems to obtain more accurate results even if the box aspect ratio is not unitary. Several examples on the box and wing aspect ratios show clearly the quartic approximation is more close to the reference results than the quadratic, for every box and wing ARs considered. In particular, quartic approximation has a good estimation of the aerodynamic damping, i.e. the imaginary part of the lift coefficient, for high box ARs and high reduced frequency. Thus, quartic approximation is more flexible and it can be used whenever a reduced amount of elements is required to limit the problem dimensions.

Moreover, accurate results have been computed by the two approximations in all the cases the box AR was limited up to 3. Such examples are the AIC matrix calculation in which no significant differences are noted.

Finally, the present collection of results has shown that the developed computer program is working correctly and, according to a huge number of papers, quartic approximation should be chosen whenever limitations on the problem dimension turn into box aspect ratios greater than 3.

References

- [1] Albano, E., and Rodden, W. P., "A Doublet-Lattice Method for Calculating Lift Distribution on Oscillating Surfaces in Subsonic Flows", *AIAA Journal*, Vol.7, 1969, pp. 279-285.
- [2] Rodden, W. P., Taylor, P. F., and McIntosh Jr., S. C., "Further Refinement of the Subsonic Doublet-Lattice Method", *Journal of Aircraft*, Vol. 35, 1998, pp. 720-727.
- [3] Vivian, H. T., and Andrew, L. V., "Unsteady Aerodynamics for Advanced Configurations. Part I – Application of the Subsonic Kernel Function to Non-Planar Lifting Surfaces", FDL-TDR-64-152, May 1965, Air Force Flight Dynamics Laboratory, Wright-Patterson Air Force Base, Ohio.
- [4] Landahl, M. T., "Kernel Function for Non-Planar Oscillating Surfaces in a Subsonic Flow", *AIAA Journal*, Vol. 5, No. 5, May 1967, pp. 1045-1046.
- [5] Hedman, S. G., "Vortex-Lattice Method for Calculation of Quasi Steady State Loadings on Thin Elastic Wing", Report 105, October 1965, Aeronautical Research Institute of Sweden.
- [6] Rodden, W. P., Giesing, J. P., and Kálmán, T. P., "New Developments and Applications of the Subsonic Doublet-Lattice Method for Non-Planar Configurations", Douglas Aircraft Company, Long Beach, USA.
- [7] Kálmán, T. P., Rodden, W. P., and Giesing, J. P., "Application of the Doublet-Lattice Method to Non-planar Configuration in Subsonic flow", Paper No. 70-539, presented to the AIAA Atmospheric Flight Conference, 13-15 May 1970, Tullahoma, Tennessee. To be published in *Journal of Aircraft*.
- [8] Rodden, W. P., Taylor, P. F., McIntosh Jr., S. C., and Baker, M. L., "Further Convergence Studies of the Enhanced Doublet-Lattice Method", *Journal of Aircraft*, Vol. 36, July-August 1999, pp. 682-688.
- [9] Chen, P. C., Liu, D. D., and Sarhaddi, D., "High-Order vs Low-Order Panel Methods for Unsteady Subsonic Lifting Surfaces", *Journal of Aircraft*, Vol. 41, No. 4, pp. 957-959.
- [10] Ueda, T., "Continuity of Lifting Surface Theory in Subsonic and Supersonic Flow", *AIAA Journal*, Vol. 36, No. 10, October 1998, pp. 1788-1791.
- [11] Chen, P. C., Silva, R. G. A., and Liu, D. D., "Transonic AIC Weighting Method using Successive Kernel Expansion", AIAA 2005-1991, 46th AIAA/ASME/ASCE/AHS/ASC Structures, Structural Dynamics & Materials Conference, 18-21 April 2005, Austin, Texas.
- [12] Richard, M., and Harrison, B. A., "A Program to Compute Three-Dimensional Subsonic Unsteady Aerodynamic Characteristics Using the Doublet Lattice Method, L216 (DUBFLX)", NASA Contractor Report 2849, Vol. I: Engineering and Usage, October 1979.
- [13] Böhm, G., and Schmid, H., "Subsonic Unsteady Airloads on Multiple Lifting Surfaces", VFW-Fokker, München, Germany.
- [14] Yates, E. C., "AGARD Standard Aeroelastic Configurations for Dynamic Response. Candidate Configuration I.-Wing 445.6", NASA Technical Memorandum 100492, August 1987.

- [15] Kier, T. M., "Comparison of Unsteady Aerodynamic Modelling Methodologies with respect to Flight Loads Analysis", AIAA Atmospheric Flight Mechanics Conference and Exhibit, 15-18 August 2005, San Francisco, California.
- [16] Arendson, P., "The B2000 Doublet Lattice Processor: B2DL", NLR-TP-2002-, October 2002.
- [17] Bisplinghoff, R. L., "Aeroelasticity", Addison Wesley Publishing Inc, Library of Congress Catalog Card 55-6561, Cambridge, Mass. 1955.
- [18] Mantegazza, P., "Determinazione delle Forze Aerodinamiche per l'Analisi Aero-Elastica delle Superfici Portanti", *L'Aerotecnica Missili e Spazio*, No 1 -2, 1976.
- [19] Rodden, W. P., and Johnson, E. H., *MSC/NASTRAN Aeroelastic Analysis User's Guide*, Version 68, The MacNeal-Schwendler Corp., 1994.
- [20] Blair, M., "A Compilation of the Mathematics Leading to the Doublet-Lattice Method", Final Report for period June 1991 – December 1991, Flight Dynamics Directorate, Air Force Wright Laboratory, Air Force System Command, Wright-Patterson Air Force Base, Ohio.
- [21] Quaranta, G., Masarati, P., and Mantegazza, P., "A conservative mesh-free approach for fluid-structure interface problems", in *International Conference on Computational Methods for Coupled Problems in Science and Engineering* (M. Papadrakakis, E. Oñate, and B. Schrefler, eds.), (Santorini, Greece), CIMNE, 2005.